International Communications in Heat and Mass Transfer 164 (2025) 108812

Contents lists available at ScienceDirect

International Communications in Heat and Mass Transfer

journal homepage: www.elsevier.com/locate/ichmt

An artificial intelligence – Finite element study of magnetohydrodynamic heat transfer of a nano-encapsulated phase change material suspension in a cylindrical enclosure with partial heated walls

Hakim S. Sultan Aljibori [a], Mohammed Hasan Ali [b], Zehba Raizah [c], Ahmad Hajjar [d], Jana Shafi [e], Faisal Alresheedi [f], Ahmed Elhassanein [g], Mohammad Edalatifar [h], Mohammad Ghalambaz [i,h,*]

[a] College of Engineering, University of Warith Al-Anbiyaa, Karbala 56001, Iraq
[b] College of Technical Engineering, Imam Ja'afar Al-Sadiq University, Al-Muthanna 66002, Iraq
[c] Department of Mathematics, Faculty of Science, King Khalid University, Abha, Saudi Arabia
[d] Center for Environmental Intelligence and College of Engineering and Computer Science, VinUniversity, Hanoi, Viet Nam
[e] Department of Computer engineering and information, College of Engineering in Wadi Alddawasir, Prince Sattam Bin Abdulaziz University, Wadi Alddawasir 11991, Saudi Arabia
[f] Department of Physics, College of Science, Qassim University, Buraidah 51452, Saudi Arabia
[g] Department of Mathematics, College of Science, University of Bisha, P.O. Box 551, Bisha 61922, Saudi Arabia
[h] Laboratory on Convective Heat and Mass Transfer, Tomsk State University, 634050 Tomsk, Russia
[i] Department of Mathematics, Saveetha School of Engineering, SIMATS, Chennai, India

ARTICLE INFO

Keywords:
Phase transition region
Nano-encapsulated phase change material suspension
Entropy
Artificial intelligence
Dataset
Point source magnetic field

ABSTRACT

The present study delivers an exhaustive exploration into the mechanisms governing heat and mass transfer within an enclosure filled with Nano-Encapsulated Phase Change Material (NEPCM) and subject to magnetic fields. Leveraging a set of governing partial differential equations, the research investigates the intricacies of natural convection, convective heat transfer, and conjugate heat transfer within solid walls. The entropy generation in the NEPCM suspension was addressed. The finite element method was used for the numerical solution. A dataset was generated from simulations and was utilized to train an artificial neural network. Subsequently, the trained neural network was employed to analyze the effects of model parameters on heat transfer and entropy generation. The results show the pivotal role of the magnetic source's position in manipulating heat transfer. Increasing the magnetic number slightly elevates Nu_{Avg} and significantly boosts total entropy generation. An increment in thermal conductivity ratio from 1 to 100 at $Ra = 100{,}000$ elevates Nu_{Avg} from 2 to 4.5, signifying a 56 % improvement. Additionally, elevating nanoparticle concentration enhances Nu_L, owing to increased thermal conductivity. The study reveals that regions of high entropy generation are universally close to the magnetic source, regardless of its specific location.

1. Introduction

In the field of thermal engineering and fluid dynamics, efficient heat transfer mechanisms hold significant importance for various applications, including electronic cooling [1], energy storage [2], and aerospace applications [3]. One innovative approach for control of heat transfer involves the use of Magnetohydrodynamics (MHD), an interdisciplinary field that couples magnetic fields with fluid flow to control heat and mass transport. An increasingly compelling avenue of research within this domain involves the use of nano-encapsulated phase change materials (NEPCMs) suspensions [4,5] as a fluid medium to capitalize on their superior thermal storage capabilities.

The interaction between magnetic fields, fluid flow, and heat transfer becomes particularly intricate when NEPCMs are introduced into the system. NEPCMs not only offer high latent heat storage but also help in uniformly distributing thermal energy, thereby minimizing thermal

* Corresponding author.
E-mail addresses: hakim.s@uowa.edu.iq (H.S.S. Aljibori), mohammed.hasan@ijsu.edu.iq (M.H. Ali), zaalrazh@kku.edu.sa (Z. Raizah), ahmad.h@vinuni.edu.vn (A. Hajjar), j.jana@psau.edu.sa (J. Shafi), f.alresheedi@qu.edu.sa (F. Alresheedi), el_hassanein@yahoo.com (A. Elhassanein), m.edalatifar@gmail.com (M. Edalatifar), m.ghalambaz@gmail.com (M. Ghalambaz).

https://doi.org/10.1016/j.icheatmasstransfer.2025.108812

Available online 9 March 2025

gradients [5,6]. When subjected to a magnetic field, the working fluid experiences Lorentz forces [7,8] that affect flow patterns and, consequently, heat transfer rates within the enclosure. As a result, the magnetic field can be harnessed to actively control and optimize thermal behavior. Here, the literature review addresses three main topics: the use of nano-additives for improving heat transfer, MHD natural convection flows, and NEPCM suspensions in enclosures.

The choice of a cylindrical enclosure with partial heated walls mimics scenarios frequently seen in industrial applications like thermal energy storge units [9] and heat exchangers [10]. In such setups, achieving homogeneous temperature distribution is critical but challenging, often demanding a precise understanding and control of fluid mechanics and thermal phenomena. The partially heated walls add a layer of complexity that requires meticulous exploration to uncover the optimal conditions for maximizing heat transfer while minimizing energy inputs. The burgeoning field of thermal engineering has increasingly turned its focus toward the behavior of nanofluids in various configurations to optimize heat transfer. Among these, natural (or free) convection heat transfer of nanofluids in enclosures (also known as cavities) has attracted particular attention for its applicability in areas ranging from electronic cooling systems to renewable energy technologies [11].

In research exploring the effects of amplitude and heat source on natural convection in a wavy enclosure, a hybrid water–Cu–Al2O3 nanofluid was utilized [12]. The study revealed that the architecture of wavy vertical surfaces within a cavity has a significant impact on the Nusselt number, a dimensionless parameter that serves as an indicator of heat transfer efficiency. Comparative analysis showed that the hybrid nanofluid yielded a 13.7 % and 5 % enhancement in average heat transfer when contrasted with pure water and other types of nanofluids, respectively. Importantly, it was noted that the length of the heat source within the enclosure had a direct influence on the Nusselt number, offering valuable insights for engineering applications where optimized heat distribution is crucial. In [13], the free convection heat transfer of nanofluids was investigated in a wavy wall enclosure. The results showed that the waving of the hot base of the cavity could augment the Nusselt number by 18 %, while the rotational speed of cylinders in the cavity could further boost it by about 315 %. These results suggest a range of strategies for dynamically controlling heat transfer in intricate systems. In a work exploring the double-diffusive magneto-natural convection of nanofluid within an enclosure equipped with a wavy porous cylinder [14], the porous medium's properties were identified as highly influential factors. In particular, heat transfer rate was found to be more sensitive to changes in the porous medium's characteristics, which suggests further avenues for manipulating thermal performance through porous material engineering.

Various aspects of MHD flows such as heat generation and non-Newtonain effects [15], mass diffusion [16], chemical reaction [17], and radiation [18], have been investigated in literature studies. Considering cavities, the impact of magnetic fields on controlling heat transfer in MHD natural convection within various enclosures (or cavities) has attracted substantial scientific interest. The application of magnetic fields significantly influences flow patterns, temperature distribution, and overall heat transfer rates, primarily by introducing Lorentz forces that counteract the buoyancy-driven flows. Several studies have elucidated the different aspects that come into play when a magnetic field is applied to such fluid flow scenarios. In a study that explored entropy generation and natural convection in a square cavity filled with Cu-Al2O3/water hybrid nanofluid, it was demonstrated that inserting a hollow conducting cylinder can significantly control the flow and heat transfer rate within the cavity [19]. This suggests that magnetic fields can effectively be used to manage the energy transport characteristics of nanofluids in enclosures. Applying a magnetic field enhances heat transfer in a fluid with Fe3O4 microparticles, significantly affecting flow and thermal properties. The magnetic field increases fluid momentum and energy exchange through Lorentz force effects and Joule heating, optimizing entropy generation and improving heat transfer efficiency by up to 8.09 % [20].

The influence of magnetic fields on heat transfer processes in fluid systems is profound, as evidenced by several studies. Research in [21] shows that increasing the Hartmann number significantly reduces real fluid velocity in a porous, asymmetric wavy channel, demonstrating the magnetic field's control over fluid dynamics. Another study [22] finds that a magnetic field decreases kinetic energy, heat, and mass transfer rates by nearly three times within the observed Hartmann number range, emphasizing its importance in applications like electronic cooling. Furthermore, [23] highlights how the orientation and intensity of the magnetic field affect Nusselt and Sherwood numbers in a staggered-shaped enclosure, pointing to strategic configuration as a method to optimize heat transfer efficiency.

It is also worth noting that entropy generation analysis provides a more comprehensive view of the system's overall efficiency. In a study focusing on a heated incinerator, it was found that the average entropy generation decreases upon applying a magnetic field, indicating enhanced system efficiency [24]. The same trend was observed in a study using a trapezoidal region with a hybrid nanoliquid under a magnetic field, where the average overall entropy generation decreased with an increase in the Hartmann number [25].

The impact of NEPCM suspensions on natural convection heat transfer in various enclosures is a research topic gaining considerable attention. NEPCMs have emerged as highly effective media for enhancing heat transfer characteristics in different types of cavities or enclosures, ranging from simple square shapes to complex adiabatic structures containing differently heated cylinder. One of the most significant impacts is the increase in overall heat transfer rates. For instance, when NEPCM particles are suspended in a complex adiabatic enclosure containing two differently heated circular cylinders, the overall heat transmission increases by up to 144.74 % when the Rayleigh number (Ra) is escalated. Conversely, growing the aspect ratio (AR) can reduce this heat transmission by up to 49 % [26]. Notably, the fusion temperature of NEPCMs can also be optimized to achieve maximum heat transfer rates. When the fusion temperature is aligned closer to the cylinder temperatures, the heat transfer decreases, suggesting that tuning the fusion temperature is crucial.

In porous, grooved cavities, NEPCMs have shown to affect streamline intensity and heat capacity position. When parameters like the Darcy parameter and Rayleigh number are adjusted, the movement and intensity of the nanofluid streamlines improve, enhancing convective heat transfer [27]. Moreover, NEPCMs contribute to fluid flow characteristics in wavy enclosures, especially when subjected to external magnetic fields [28]. The magnetic influence can deter energy transference as it makes conduction the dominant mode of heat transfer. However, a higher Rayleigh number can offset this by increasing the Nusselt number, making the system more efficient in terms of convective heat transfer [29]. The presence of NEPCM particles also amplifies heat transfer over vertical flat plates embedded in porous media [30]. Interestingly, a lower fusion temperature of the NEPCM cores can significantly enhance this heat transfer. A mere 5 % addition of NEPCM particles can enhance the heat transfer parameter by about 25 %, compared to cases with no NEPCM particles. The versatility of NEPCMs also extends to their application in double-diffusive convection flows inside a compound cavity with a rotating cylinder. The fusion temperature governs the location and intensity of the phase change zone inside the cavity, providing another layer of control over heat transfer properties [31]. In enclosures with discrete heat sources, increasing the NEPCM concentration notably elevates the maximum Nusselt number [32]. Furthermore, rotational parameters can modulate the heat transfer rates in a square enclosure filled with a heterogeneous mixture of NEPCMs and water, offering opportunities for fine-tuning thermal management systems [33].

The existing body of literature extensively explores the natural convection heat transfer within enclosures, facilitated by both single-

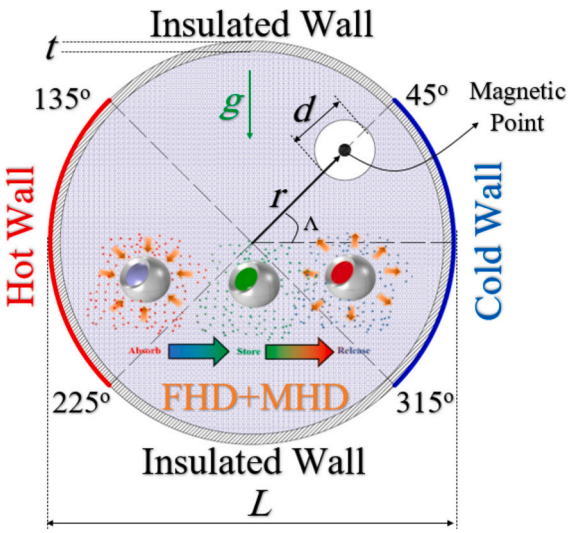

Fig. 1. Graphic outline of the theoretical model.

component and hybrid nanoparticles. Unlike conventional nanoparticles that remain thermally stable across their operational temperature range, NEPCM nanoparticles feature a core capable of undergoing phase transitions. This unique characteristic enables NEPCMs to significantly impact heat transfer, thanks to the latent heat of phase change at a relatively stable fusion temperature. In addition, previous studies have highlighted the role of magnetic fields in modulating both fluid flow and heat transfer rates within enclosures. However, an unexplored area within this field is the thermal behavior of NEPCM suspensions when subjected to localized magnetic fields. This is particularly intriguing given that NEPCMs are a burgeoning class of nanomaterials, and their specific interactions with magnetic fields could offer new avenues for thermal management solutions. To bridge this gap, the present study pioneers an investigation into the fluid dynamics and heat transfer properties of NEPCM suspensions under the influence of a point source magnetic field. The present study, for the first time, aims to address the flow and heat transfer of NEPCM suspensions subject to a point source magnetic field in a cylindrical enclosure with partially heated walls.

2. Mathematical model and formulation

2.1. Mathematical model

The present study introduces a mathematical model designed to investigate thermophysical interactions within a cylindrical enclosure saturated with NEPCM. As illustrated in Fig. 1, the enclosure has a diameter of L and wall thickness of t. Within this enclosure, a magnetic source is positioned, mounted on a circuit with a radius of r and encased within a sleeve of diameter d. The magnetic field is generated by a wire that extends along the third dimension of the enclosure. Thus, the 2D model represents the natural convection within the cavity, distant from the effects of the third-dimensional walls. These assumptions are explained in the model description for clarification. This inclusion allows for an in-depth understanding of conjugate natural convection heat transfer phenomena influenced by magnetic fields.

The walls of the enclosure are divided into hot and cold sections situated on the left and right sides, respectively, each covering half of the enclosure's perimeter. The remaining walls are treated as perfectly insulated. The magnetic source is configured to induce Ferrohydrodynamic (FHD) and MHD effects within the NEPCM. Lorentz and Kelvin forces, arising from the magnetic field are explicitly included in the governing equations, thereby capturing the intricate physics of the system. These forces are observed to generate unique flow patterns and heat transfer mechanisms, which are considered essential for various practical applications.

Joule-heating and Magneto-Caloric effects, emanating from viscous dissipation terms, are also incorporated into the model. These elements play a critical role in evaluating the effectiveness and efficiency of thermal storage in the system. Further, entropy generation within the enclosure is calculated to provide insights into thermodynamic inefficiencies and avenues for optimization. Water boiling and freezing can impact the nanoparticles' stability and thermal cycling. Thus, in the present study, the temperature differences are limited, and the thermophysical properties can be assumed constant except for the buoyancy forces, which were modeled using the Boussinesq approximation.

The Boussinesq approximation is employed for simulating buoyancy-driven flow due to temperature gradients within the enclosure. The cylindrical enclosure with magnetic source represents a current-carrying wire through a pipe where the pipe is filled with NEPCM suspension and subject to temperature difference with environment.

In the model, most thermophysical properties of the NEPCM are held constant, with the exception of heat capacity, which is modulated to account for latent heat during phase changes. This feature allows for a realistic portrayal of thermal storage capabilities. Overall, it is believed that the model offers a comprehensive framework for analyzing thermal systems utilizing NEPCM and influenced by magnetic fields. By encapsulating complex interactions between heat and mass transfer, phase changes, and magnetic effects, the model aims to serve as a foundation for the development of more efficient thermal storage systems.

2.2. Mathematical formulation

The mathematical framework presented in this study encompasses a multi-faceted approach to modeling heat and mass transfer phenomena. Specifically, it addresses fluid dynamics resulting from natural convection, convective heat transfer in the domain filled with NEPCM suspension, as well as conjugate heat transfer occurring within the solid walls of the enclosure. In this way, the model captures both the fluidic and solid-state aspects of thermal systems, thereby providing a more comprehensive view of the heat transfer processes.

The governing equations for this system are formulated as partial differential equations (PDEs), enabling an intricate depiction of the variables and their interactions over space and time. These PDEs account for the momentum, energy, and mass transfer in both the fluid and solid domains, thereby offering a unified model that encapsulates a broad range of thermal phenomena. By including natural convection, the study considers the buoyancy-driven flow arising from temperature gradients within the NEPCM-filled enclosure. This is particularly significant for applications where passive heat transfer mechanisms are desired. Convective heat transfer in the NEPCM fluid domain, on the other hand, allows for a more accurate understanding of how the encapsulated phase change material contributes to thermal storage and energy efficiency. Lastly, the conjugate heat transfer in the solid walls captures the interfacial thermal interactions between the solid wall and the adjacent fluid, which is vital for a realistic representation of heat flow in systems where the wall material itself may have significant thermal mass or insulating properties.

Thus, the governing equations in their PDE form serve as the mathematical backbone for simulating and understanding the complex, multi-physical phenomena inherent in systems involving fluid flows, latent heat thermal energy storage, as well as melting and solidification processes. The governing equations for the current model can be represented as [34–36]:

Continuity

$$\frac{\partial u}{\partial x}+\frac{\partial v}{\partial y}=0 \tag{1}$$

Momentum

Table 1
Utilized equations for determining the thermophysical properties of the suspension.

Suspension properties	Ref.	Relationship	Eq.
Specific heat capacity	[38,39]	$Cp_{npcm} = \left(\rho_{fluid} Cp_{fluid}(1-\varphi) + \rho_{particle} Cp_{particle}\varphi\right)\rho_{npcm}^{-1}$	(9)
Particles' density	[40]	$\rho_{particle} = (\rho_{core}\rho_{shell})(1+\iota)/(\iota\rho_{core} + \rho_{shell})$	(10)
Density	[40]	$\rho_{npcm} = \varphi\rho_{particle} + (1-\varphi)\rho_{fluid}$	(11)
Thermal expansion	[41]	$\beta_{npcm} = \varphi\beta_{particle} + (1-\varphi)\beta_{fluid}$	(12)
Particles' core specific heat capacity	[40,41]	$Cp_{particle} = Cp_{core} + \zeta\left\{\frac{\pi}{2}\left(\frac{h_{sf}}{T_{\delta T}} - Cp_{core}\right) sin\left(\pi\frac{T - T_f + \delta T/2}{\delta T}\right)\right\}$	(13)
Phase change profile	[40,41]	$\zeta = \begin{cases} 0 & T < Tm - \delta T/2 \\ 1 & Tm - \delta T/2 < T < Tm + \delta T/2 \\ 0 & T > Tm + \delta T/2 \end{cases}$	(14)
Dynamic viscosity	[36,42,43]	$\frac{\mu_{npcm}}{\mu_{fluid}} = 1 + N\nu\varphi$	(15)
Thermal conductivity	[36,42,43]	$\frac{k_{npcm}}{k_{fluid}} = 1 + Nc\varphi$	(16)
Electrical conductivity	[35]	$\frac{\sigma_{npcm}}{\sigma_{fluid}} = 1 + \frac{3\left(\frac{\sigma_{particle}}{\sigma_{fluid}} - 1\right)\varphi}{\left(2 + \frac{\sigma_{particle}}{\sigma_{fluid}}\right) - \left(\frac{\sigma_{particle}}{\sigma_{fluid}} - 1\right)\varphi}$	(17)

$$\rho_{nf}\left(u\frac{\partial u}{\partial x} + v\frac{\partial u}{\partial y}\right) = -\frac{\partial p}{\partial x} + \mu_{nf}\left(\frac{\partial^2 u}{\partial x^2} + \frac{\partial^2 u}{\partial y^2}\right) + \mu_0 M\frac{\partial h}{\partial x} - \sigma_{nf}B_y^2 u + \sigma_{nf}B_x B_y v \tag{2}$$

$$\rho_{nf}\left(u\frac{\partial v}{\partial x} + v\frac{\partial v}{\partial y}\right) = -\frac{\partial p}{\partial y} + \mu_{nf}\left(\frac{\partial^2 v}{\partial x^2} + \frac{\partial^2 v}{\partial y^2}\right) + g\rho_{nf}\beta_{nf}(T - T_c) + \mu_0 M\frac{\partial h}{\partial y} - \sigma_{nf}B_x^2 v + \sigma_{nf}B_x B_y u \tag{3}$$

Convective heat transfer

$$(\rho C_p)_{nf}\left(u\frac{\partial T}{\partial x} + v\frac{\partial T}{\partial y}\right) = k_{nf}\left(\frac{\partial^2 T}{\partial x^2} + \frac{\partial^2 T}{\partial y^2}\right) + \sigma_{nf}\left(uB_y - vB_x\right)^2 - \mu_0 T\frac{\partial M^*}{\partial T}\left(u\frac{\partial h}{\partial x} + v\frac{\partial h}{\partial y}\right) \tag{4}$$

Conduction heat transfer in solid wall

$$k_s\left(\frac{\partial^2 T}{\partial x^2} + \frac{\partial^2 T}{\partial y^2}\right) = 0 \tag{5}$$

The magnetic source definition

$$h^*(x,y) = \frac{I}{2\pi\varsigma}\delta \tag{6-a}$$

$$h_x^*(x,y) = \frac{I}{2\pi}\frac{y + d_1}{\varsigma^2}, h_y^*(x,y) = -\frac{I}{2\pi}\frac{x + d_2}{\varsigma^2} \tag{6-b}$$

$$h^*(x,y) = \sqrt{h_x^{*2} + h_y^{*2}} \tag{6-c}$$

$$\varsigma = \sqrt{(x + d_2)^2 + (y + d_1)^2}, \delta = \frac{y + d_1}{\varsigma}i - \frac{x + d_2}{\varsigma}j \left| \begin{array}{l} d_1 = rsin(\Lambda) \\ d_2 = rcos(\Lambda) \end{array} \right. \tag{6-d}$$

The boundary conditions in a mathematical format can be written as:

$$\text{on } \frac{L}{2} \left| \begin{array}{l} 135^o \le \Lambda \le 225^o \rightarrow T = T_h \\ 315^o(-45^o) \le \Lambda \le 45^o \rightarrow T = T_c \end{array} \right. , \quad u = v = 0 \tag{7-a}$$

$$\text{on } \frac{L}{2} \left| \begin{array}{l} 45^o \le \Lambda \le 135^o \\ 225^o \le \Lambda \le 315^o \end{array} \right. \rightarrow \frac{\partial T}{\partial n} = 0 \quad , \quad u = v = 0 \tag{7-b}$$

$$on\left(\frac{L}{2} - t\right) \left| \begin{array}{l} 135^o \le \Lambda \le 225^o \\ 315^o(-45^o) \le \Lambda \le 45^o \end{array} \right. \rightarrow k_s\frac{\partial T}{\partial n}\bigg|_s = k_b\frac{\partial T}{\partial n}\bigg|_b, u = v = 0 \tag{7-c}$$

The equation outlined below illustrates the methodology for calculating entropy production, which incorporates both localized thermal entropy generation, as well as localized frictional entropy generation:

$$s_l = s_{thermal} + s_{friction} = \frac{k_{npcm}}{T_0^2}\left[\left(\frac{\partial T}{\partial x}\right)^2 + \left(\frac{\partial T}{\partial y}\right)^2\right] + \frac{\mu_{npcm}}{T_0}\left(2\left(\left(\frac{\partial u}{\partial x}\right)^2 + \left(\frac{\partial v}{\partial y}\right)^2\right) + \left(\frac{\partial u}{\partial y} + \frac{\partial v}{\partial x}\right)^2\right) \tag{8}$$

Within this equation, the terms s_{thermal} and s_{friction} are utilized to specify the generation of entropy arising from gradients in temperature and inter-layer fluid friction, respectively.

2.3. The suspension thermo-physical properties

The suspension's thermophysical properties are computed using relationships provided in literature as summarized in Table 1. Here, φ denotes the volume fraction of NEPCM particles. The ratio of mass between the core and the shell, denoted as ι, is approximately set at a value of 0.447, as cited in reference [37]. To ensure a consistent energy balance, the phase transition temperature range, represented by δT, is chosen such that $\delta T/(Th\text{-}Tc)$ equals 0.05, according to reference [36]. Furthermore, the term h_{sf} is utilized to indicate the latent heat corresponding to the cores of the NEPCM particles.

2.4. Scaled equations

The governing equations can be scaled into a dimensionless form using the following scaled parameters:

$$(X, Y, D_1, D_2) = \frac{(x, y, d_1, d_2)}{L}, \; U = \frac{uL}{\alpha_{fluid}}, V = \frac{vL}{\alpha_{fluid}}, P = \frac{pL^2}{\rho_{fluid}\alpha_{fluid}^2}, \quad \theta = \frac{T - T_c}{T_h - T_c}, H = \frac{h^*}{H_0}, \; H_x = \frac{h_x^*}{H_0}, H_y = \frac{h_y^*}{H_0}, \theta_m = \frac{T_m - T_c}{(T_h - T_c)} \tag{18}$$

where $H_0 = H^*(d_2, d_1) = \frac{\gamma}{2\pi L}$. As a result, the dimensionless format of the governing equations is obtained as:

$$\frac{\partial U}{\partial X} + \frac{\partial V}{\partial Y} = 0 \tag{19}$$

$$U\frac{\partial U}{\partial X}+V\frac{\partial U}{\partial Y}=-\frac{\rho_{fluid}}{\rho_{npcm}}\frac{\partial P}{\partial X}+\frac{\rho_{fluid}}{\rho_{npcm}}MnfH\frac{\partial H}{\partial X}(\varepsilon_2-\varepsilon_1-\theta)+ \frac{\sigma_{npcm}}{\sigma_{fluid}}\frac{\rho_{fluid}}{\rho_{npcm}}Ha^2Pr\left(H_xH_yV-H_y^2U\right)+\frac{\rho_{fluid}}{\rho_{npcm}}\frac{\mu_{npcm}}{\mu_{fluid}}Pr\left(\frac{\partial^2U}{\partial X^2}+\frac{\partial^2U}{\partial Y^2}\right) \tag{20}$$

$$U\frac{\partial V}{\partial X}+V\frac{\partial V}{\partial Y}=-\frac{\rho_{fluid}}{\rho_{npcm}}\frac{\partial P}{\partial Y}+\frac{\rho_{fluid}}{\rho_{npcm}}MnfH\frac{\partial H}{\partial Y}(\varepsilon_2-\varepsilon_1-\theta)+ \frac{\sigma_{npcm}}{\sigma_{fluid}}\frac{\rho_{fluid}}{\rho_{npcm}}Ha^2Pr\left(H_xH_yU-H_x^2V\right)+\frac{\rho_{fluid}}{\rho_{npcm}}\frac{\mu_{npcm}}{\mu_{fluid}}Pr\left(\frac{\partial^2V}{\partial X^2}+\frac{\partial^2V}{\partial Y^2}\right)+ \frac{\beta_{fluid}}{\beta_{npcm}}RaPr\theta \tag{21}$$

$$Cr\left(U\frac{\partial\theta}{\partial x}+V\frac{\partial\theta}{\partial y}\right)=\frac{k_{npcm}}{k_{fluid}}\left(\frac{\partial^2\theta}{\partial X^2}+\frac{\partial^2\theta}{\partial Y^2}\right)+\frac{\sigma_{npcm}}{\sigma_{fluid}}Ha^2Ec\left(UH_y-VH_x\right)^2 +EcMnfH(\theta+\varepsilon_1)\left(U\frac{\partial H}{\partial X}+V\frac{\partial H}{\partial Y}\right) \tag{21}$$

The energy equation for the solid block is:

$$0=R_k\left(\frac{\partial^2\theta}{\partial X^2}+\frac{\partial^2\theta}{\partial Y^2}\right)\ \Big|\ R_k=\frac{k_s}{k_{fluid}} \tag{23}$$

in the above equations, the dimensionless parameters are:

$$\varepsilon_1=\frac{T_c}{\Delta T},\varepsilon_2=\frac{T_c'}{\Delta T},Ra=\frac{g\rho_{fluid}\beta_{fluid}\Delta TL^3}{\alpha_{fluid}\mu_{fluid}},Mnf=\frac{\mu_0H_0^2k'\Delta TL^2}{\mu_{fluid}\alpha_{fluid}}, Ec=\frac{\mu_{fluid}\alpha_{fluid}}{L^2(\rho c_p)_{fluid}\Delta T},Pr=\frac{\mu_{fluid}}{\rho_{fluid}\alpha_{fluid}},Ha=\mu_0LH_0\sqrt{\frac{\sigma_{fluid}}{\mu_{fluid}}} \tag{24}$$

where

$$Cr=\frac{(\rho C_p)_{nf}}{(\rho C_p)_{bf}}=(1-\varphi)+\varphi\lambda+\frac{\varphi}{\delta Ste}f \tag{25}$$

Cr represents the heat capacity ratio of the suspension to the base fluid. Moreover, the variables including the heat capacity ratio, denoted as λ, the scaled phase transition range symbolized by δ, and the Stefan number, indicated as *Ste*, are all introduced as follows:

$$\delta=\frac{T_{Mr}}{\Delta T},Ste=\frac{(\rho Cp)_{fluid}\Delta T(\rho_{sell}+\iota\rho_{core})}{\alpha_{fluid}(h_{sf}\rho_{core}\rho_{sell})},\lambda=\frac{(Cp_{core,l}+\iota Cp_{shell})\rho_{core}\rho_{shell}}{(\rho Cp)_{fluid}(\rho_{sell}+\iota\rho_{core})} \tag{26}$$

Also, the scaled fusion function (f) is introduced as:

$$f=\frac{\pi}{2}sin\left[\left(\frac{\delta}{2}+\theta-\theta_m\right)\frac{\pi}{\delta}\right]\times\begin{cases}0 & \theta<\theta_m-\delta/2\\ 1 & \theta_m-\delta/2<\theta<\theta_f+\delta/2\\ 0 & \theta>\theta_m+\delta/2\end{cases} \tag{27}$$

where the scaled fusion temperature (θ_f) is:

$$\theta_f=\frac{T_m-T_c}{\Delta T} \tag{28}$$

The applied boundary conditions can be articulated in a dimensionless manner:

$$on\ \frac{1}{2}\ \Big|\ \begin{matrix}135^o\le\Lambda\le225^o\rightarrow\theta=1\\ 315^o(-45^o)\le\Lambda\le45^o\rightarrow\theta=0\end{matrix}\quad,\quad U=V=0 \tag{29-a}$$

$$on\ \frac{1}{2}\ \Big|\ \begin{matrix}45^o\le\Lambda\le135^o\\ 225^o\le\Lambda\le315^o\end{matrix}\rightarrow\frac{\partial\theta}{\partial N}=0\quad,\quad U=V=0 \tag{29-b}$$

$$on\left(\frac{1}{2}-\tau\right)\ \Big|\ \begin{matrix}135^o\le\Lambda\le225^o\\ 315^o(-45^o)\le\Lambda\le45^o\end{matrix}\rightarrow R_k\frac{\partial\theta}{\partial N}\Big|_s=\frac{\partial\theta}{\partial N}\Big|_b,U=V=0 \tag{29-c}$$

2.5. The entropy generation and streamlines

The relation for entropy generation can be expressed in a dimensionless form:

$$S_T=S_\theta+S_\psi=\frac{k_{npcm}}{k_{fluid}}\left[\left(\frac{\partial\theta}{\partial X}\right)^2+\left(\frac{\partial\theta}{\partial Y}\right)^2\right]+\chi_0\frac{\mu_{npcm}}{\mu_{fluid}}\left(2\left(\frac{\partial U}{\partial X}\right)^2+2\left(\frac{\partial V}{\partial Y}\right)^2+\left(\frac{\partial U}{\partial Y}+\frac{\partial V}{\partial X}\right)^2\right) \tag{30}$$

in which χ_0 denotes the irreversibility parameter introduced as:

$$\chi_0=\frac{\mu_{fluid}T_0}{k_{fluid}}\left(\frac{\alpha_{fluid}}{L(T_h-T_c)}\right)^2 \tag{31}$$

$$Entropy=\frac{\oint_A S_T dA}{A} \tag{32}$$

Eventually, the dimensionless streamline (ω) is introduced as:

$$\nabla^2\omega=\left(\frac{\partial U}{\partial Y}-\frac{\partial V}{\partial X}\right) \tag{33}$$

in which $U=\partial\omega/\partial Y$ and $V=-\partial\omega/\partial X$. and $\omega=0$ was applied at the enclosure surfaces as [44,45].

2.6. Rate of heat transfer

The local heat transfer rates entering the cavity via the hot wall are determined through the following equation:

$$Nu_{Local}=-R_k\left(\frac{\partial\theta}{\partial N}\right)_{on\ \frac{1}{2}\rightarrow135^o\le\Lambda\le225^o} \tag{34}$$

Additionally, the formula for the average Nusselt number associated with the hot wall can be expressed as follows:

$$Nu_{Avg}=\int-R_k\left(\frac{\partial\theta}{\partial N}\right)_{on\ \frac{1}{2}\rightarrow135^o\le\Lambda\le225^o}dN \tag{35}$$

which *N* is surface normal and integration takes place over the length of the heated wall.

3. Solution method, mesh sensitivity analysis, and model verification

3.1. Solution method

The Finite Element Method (FEM) was utilized to unravel the governing equations, along with their associated initial and boundary conditions. This computational approach demonstrated efficacy in addressing the non-linear sink/source terms that arise due to phase transitions, as noted in works by Zienkiewicz et al. [46] and Pepper [47]. By applying a weak formulation of the principal equations and employing a second-order approximation for the equations governing heat and momentum, algebraic residual equations were generated using Gauss quadrature integration at the elemental level.

For the iterative and coupled solution of these equations, the Newton technique was invoked, referencing methodologies from Kelley [48] and Deuflhard [49]. To enhance convergence rates, a damping coefficient set at 0.8 was incorporated into the calculations. In conjunction with the Newton technique, the PARDISO parallel solver was leveraged to enable parallel computations across multiple processing units, as cited in studies by [50,51]. A threshold for relative solution accuracy was set at less than 10^{-4} for all computational analyses.

Table 2
Impact of mesh elements on average Nusselt number.

Case No.	Mesh quality	Mesh quantity (Overall number of Elements)	Nu_t	*Err* (%)
1	Normal	1678	2.9473	8.55
2	Fine	2462	2.7152	4.85
3	Finer	7176	2.8536	3.21
4	**Extra Fine**	**19,434**	**2.9481**	**0.26**
5	Extremely fine	24,380	2.9404	–

Bold row shows the selected mesh size for computations.

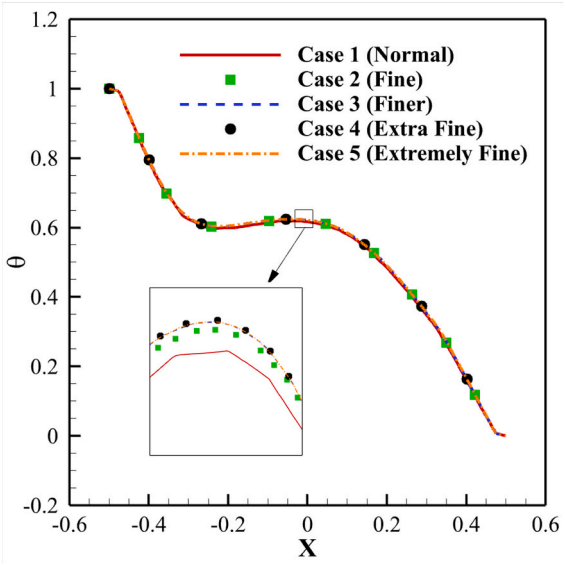

Fig. 2. Temperature at mid-plane of the enclosure at $Y = 0$ for various evaluated meshes.

3.2. Mesh sensitivity analysis

The mesh analysis is undertaken for a specific test case characterized by a set of predefined parameters: $Ra = 10^5$, $R_k = 10$, $\theta_f = 0.3$, $Ste = 0.3$ $Pr = 6.2$, $Mnf = 50$, $Ha = 20$, $Nc = 6$, $Nv = 6$, $\varphi = 0.05$, and $Ec = 10^{-5}$. In Table 2, five different mesh sizes are compared: Normal, Fine, Finer, Extra Fine, and Extremely Fine. These mesh sizes correspond to overall element counts of 1678, 2462, 7176, 19,434, and 24,380, respectively. One of the critical outcomes presented is the Average Nusselt number (Nut), a dimensionless number used to quantify heat transfer. Associated with each mesh size is also an error percentage (Err %) which gives an idea of the relative computational error incurred by that particular mesh resolution.

As the table reveals, the error decreases progressively as the mesh becomes finer. Starting with an 8.55 % error at a normal mesh size (1678 elements), it shrinks to a negligible 0.26 % for the Extra Fine mesh (19,434 elements). Interestingly, the Extremely Fine mesh with 24,380 elements, which is selected as the optimal size for computations, shows a Nusselt number (2.9404) quite close to that achieved with the Extra Fine mesh, but the error percentage is not provided, possibly implying near-perfect accuracy.

Furthermore, it is worth noting that the local Nusselt number is also

Fig. 4. Isotherm Comparison: (a) Results from the current study, and (b) Observations reported in [52].

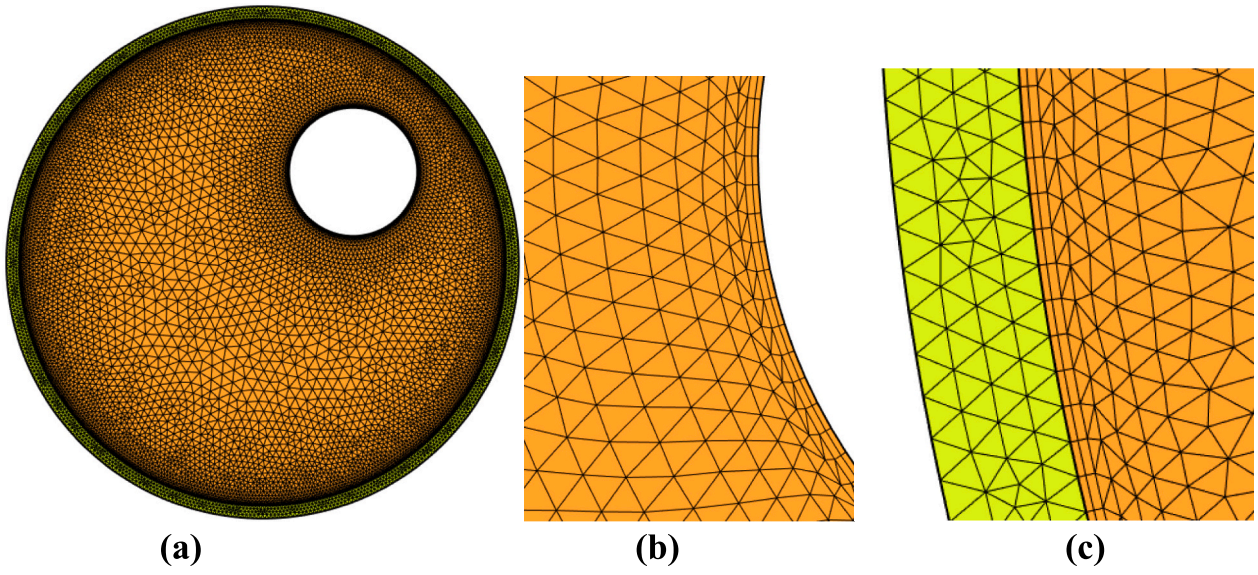

Fig. 3. A view of utilized mesh: (a) overall view of the mesh, (b) a zoomed view close to the sleeve, and (c) a zoomed view close to the solid wall.

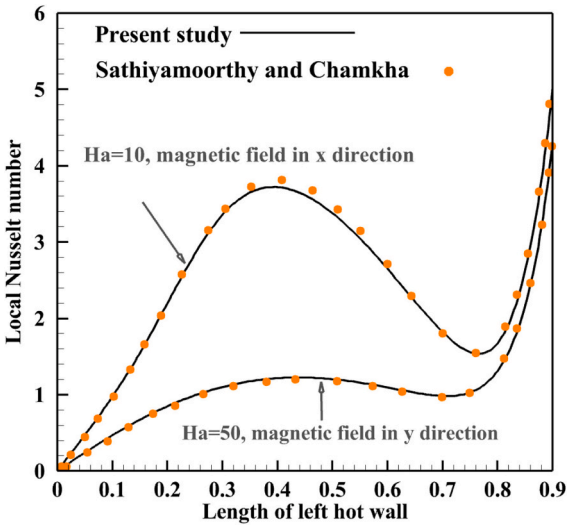

Fig. 5. Local Nusselt number comparison computed by the present study and those reported in [8].

depicted in Fig. 2, focusing on variations along the hot wall, thereby complementing the average Nusselt number data in Table 2. This comprehensive analysis aids in choosing the appropriate mesh size for achieving optimal computational accuracy in the simulation of complex fluid and thermal phenomena. Fig. 3 provides a visual representation of the mesh employed for Case 4. While Fig. 3(a) offers an overview of the entire mesh structure, Fig. 3(b) and (c) present magnified views adjacent to the walls. Boundary-layer-shaped meshes are specifically utilized in these areas to more accurately capture variations in both flow and temperature gradients.

3.3. Model verification

A validation of the current study's findings is established through a comparative analysis with the results shown in [52], as illustrated in Fig. 4. An experimental study by Goldstein and Kuehn [52] aimed to broaden the understanding of heat transfer and fluid flow characteristics within a horizontal annulus. The strong correlation between the numerical outcomes of this study and the experimental data from Goldstein and Kuehn [52] underscores the reliability and accuracy of the code employed in the present work.

Researchers in [8] examined the interaction of natural convection heat transfer with magnetohydrodynamic flows inside a chamber, using various heating methods and applying a uniform magnetic field. The study follows the Rayleigh number setting of $Ra = 105$, as established by [8], for comparison. The local Nusselt number is depicted in Fig. 5 for Hartmann numbers $Ha = 10$ and $Ha = 50$, where the data points are derived from [8] and the lines represent findings from the current study.

In another study [36], the investigation focused on the behavior of free convection in NEPCM suspensions within a square enclosure, featuring a hot left wall and a cold right wall, while the top and bottom walls were insulated. The research employed CR contours, isotherms, and streamlines to depict field variables. The analysis was performed under conditions including $Ra = 10^5$, $\theta_f = 0.3$, $Pr = 6.2$, $Ec = Ha = 0$, $\kappa = 0.33$, Ste. $= 0.3$, $Nc = 23.8$, $Nv = 12.5$, and $\varphi = 0.05$, with a density ratio

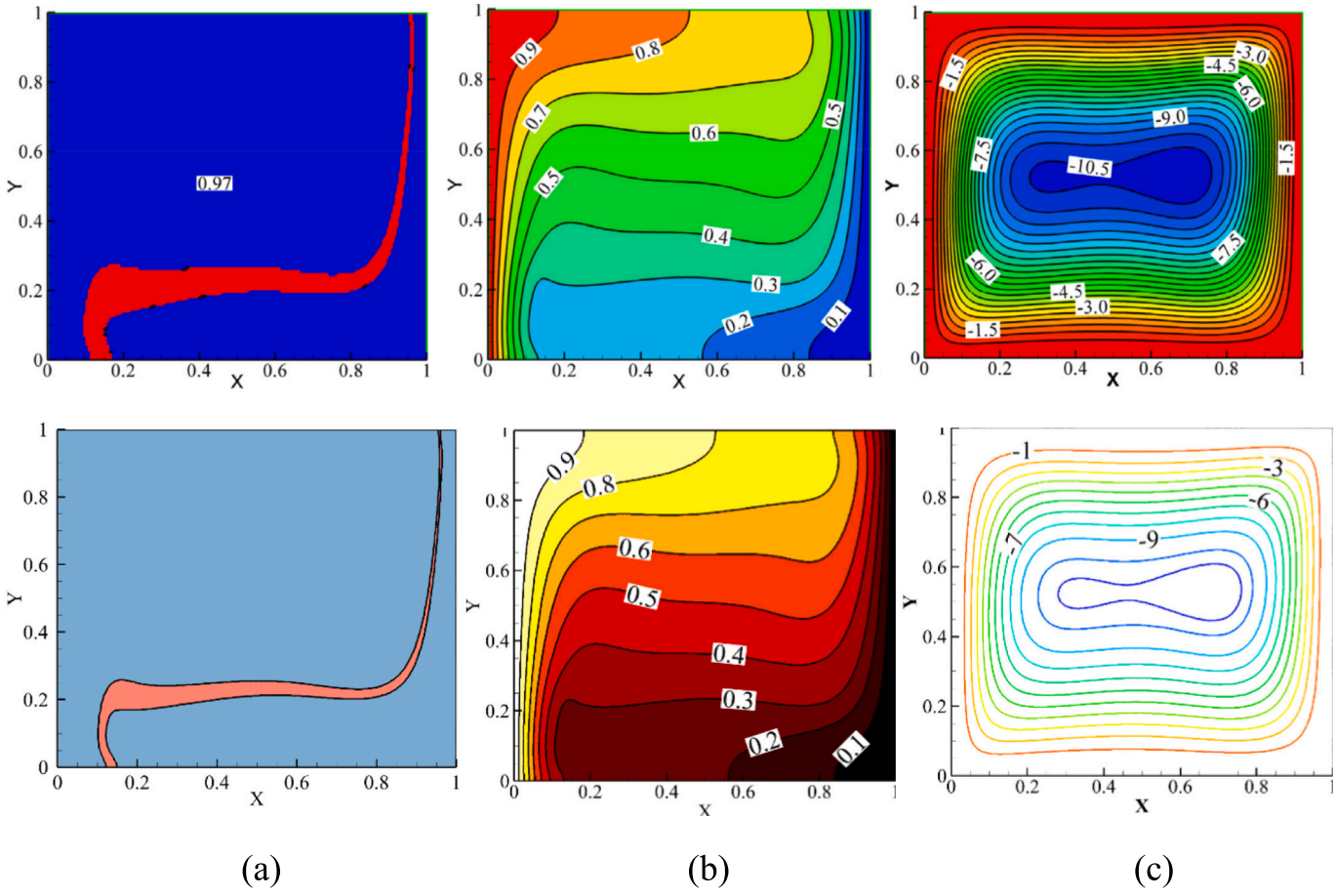

Fig. 6. Comparison between the results of the present study (first row) and those of the present study (second row) for (a) the phase transition (Cr), (b) temperature contours, and stream functions of [36].

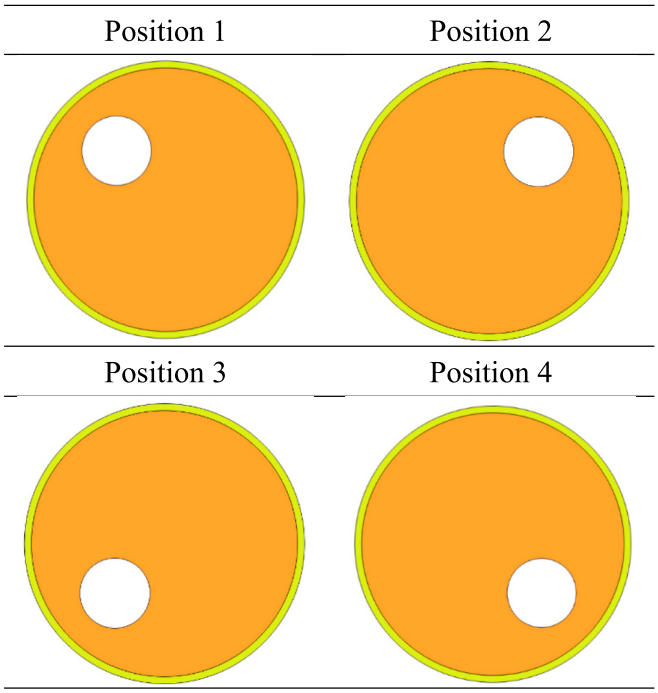

Fig. 7. A schematic view of magnetic source position.

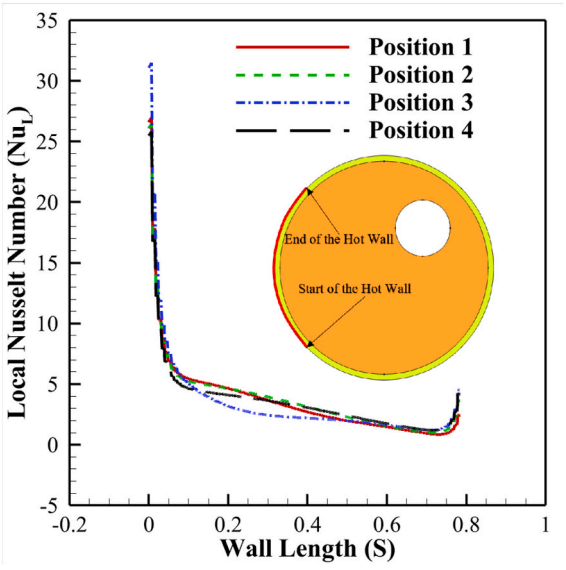

Fig. 8. Effect of magnetic source position on the local Nusselt number (Nu_L).

of $\rho_p/\rho_f = 0.9$. Fig. 6 shows a comparison of the current study's results with those from [36], highlighting the significant congruence that supports the reliability of the current study's simulations.

4. Results and discussions

In the present study, the impacts of the location of the magnetic source, magnetic number ($0 < Mnf < 500$), Hartmann number ($0 < Ha < 60$), Rayleigh number ($0 < Ra \langle 100{,}000$), thermal conductivity ratio ($1 < R_k \langle 100$), Nanoparticles fusion temperature ($0.1 < \theta_f < 0.9$), and the nanoparticles' concentration ($0 < \varphi < 0.05$) were addressed on heat transfer and entropy generation of NEPCM suspensions in the enclosure subject to a magnetic field. The values of non-dimensional parameters were considered identical to the mesh study case, and otherwise, the value of a parameter will be stated.

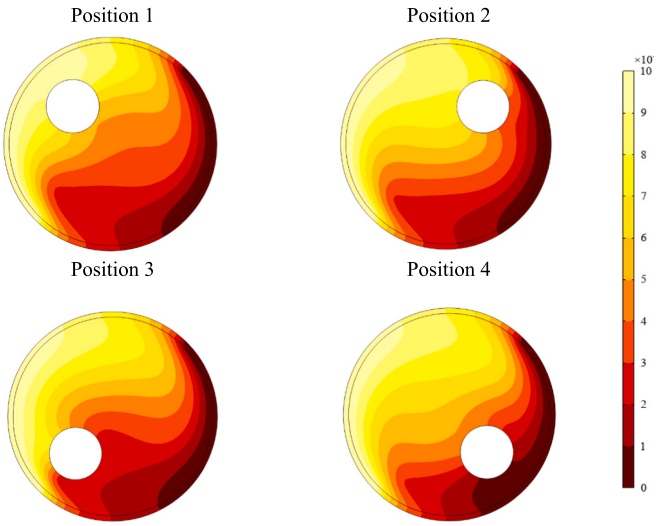

Fig. 9. Impact of magnetic source location on temperature contours.

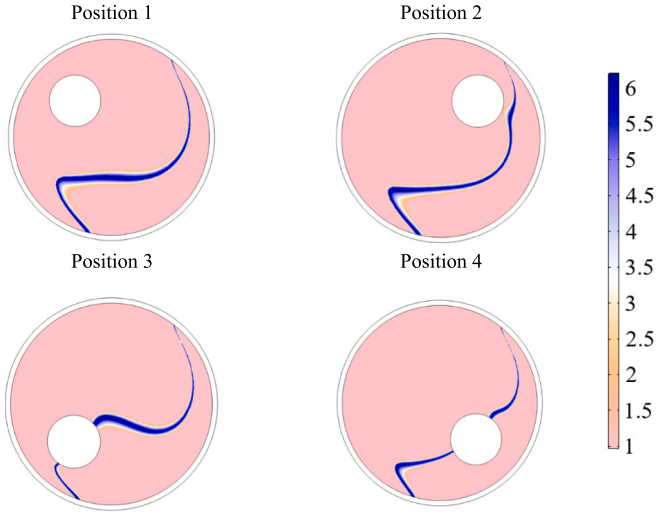

Fig. 10. Impact of magnetic source location on phase transition maps.

4.1. Numerical simulation results

In the current study, Fig. 7 provides a detailed schematic illustrating the various positions of the magnetic source being investigated. Specifically, the magnetic source can be strategically placed in one of four quadrants: top-left (Position 1), top-right (Position 2), bottom-left (Position 3), and bottom-right (Position 4).

Fig. 8 shows the substantial influence exerted by the magnetic source's position on the local Nusselt number (Nu_L) along the hot wall. Initial contact with the cold suspension propels Nu_L to significant levels at the commencement of the hot wall. Thereafter, Nu_L experiences a rapid decline as a thermal gradient establishes itself across the hot wall. It becomes glaringly apparent that the magnetic source's positioning has a pronounced impact on Nu_L, particularly when located at the bottom-left quadrant (Position 3). Here, the magnetic source is not only proximate to the hot wall but also plays a pivotal role in directing the flow of incoming cold suspension toward it. This position noticeably dampens the Nu_L at the midpoint of the hot wall's length by inhibiting fluid flow over the hot wall. Conversely, the magnetic source's influence on Nu_L is comparatively less pronounced when positioned elsewhere.

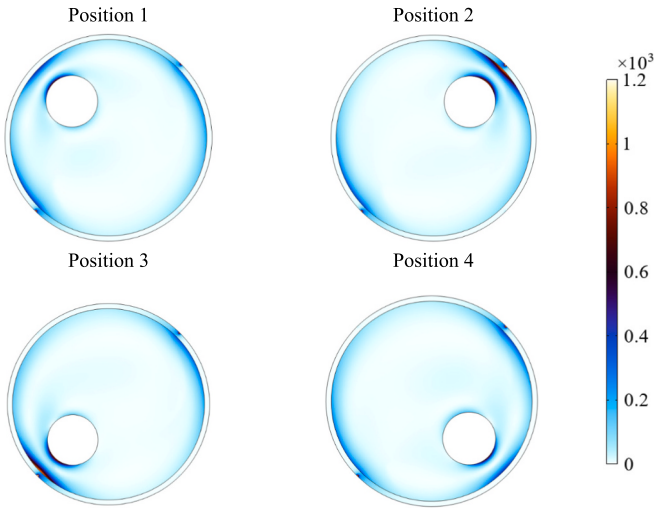

Fig. 11. Impact of magnetic source location on entropy generation contours.

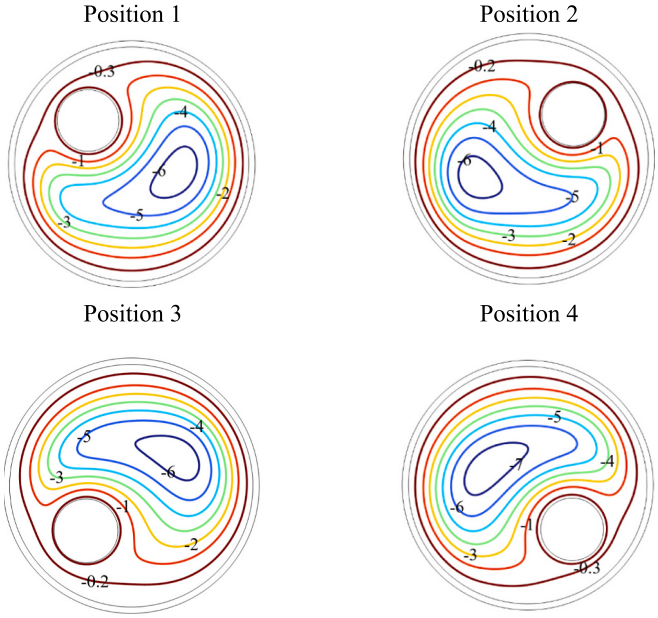

Fig. 12. Impact of magnetic source location on streamlines.

Figs. 9 through 12 sequentially explore how the magnetic field's location affects various critical parameters: temperature contours, phase transition maps, entropy generation, and flow streamlines. When the magnetic source occupies the bottom-left quadrant (Position 3), the isotherms experience notable deflection toward the heated wall, thereby attenuating adjacent temperature gradients. This altered isothermal profile, in turn, shifts the phase transition region away from the hot wall and toward its cold counterpart. The streamlines are distanced apart, indicating lower flow rates near the hot wall—a finding that aligns closely with the Nu_L observations presented in Fig. 8. As the streamlines get closer, the velocity magnitude increases. Around the cylinder, the streamlines are quite distant, indicating low velocity due to cylinder skin friction and pressure resistance against fluid movement. In the center of the enclosure, the streamlines are also distant. The greatest concentration of streamlines can be seen within close proximity to the walls, where temperature differences and buoyancy forces are high, but wall effects keep the fluid at zero velocity at the wall. Thus, just next to the wall, a natural convection flow forms.

Entropy generation is most evident near the initial portions of both hot and cold walls, particularly in zones where convective flows intersect regions of significant temperature gradients. Irrespective of the magnetic source's specific location, a region of high entropy generation is consistently observed in close proximity to the magnetic circle. This can be attributed to the attenuated flow velocities in that area, which result in extended temperature gradients and, consequently, reduced entropy generation.

Fig. 13 illuminates the consequential effects of varying the Hartmann number (*Ha*) and magnetic parameter on two crucial metrics: the average Nusselt number (Nu_{Avg}) and total entropy generation (E_T). Upon an increase in the Hartmann number, both Nu_{Avg} and E_T experience a reduction. The underlying mechanism for this behavior stems from the induced local Lorentz force that arises with an augmented *Ha*. This force effectively acts as a resistance against fluid motion, thereby attenuating the vigor of natural convection flows within the enclosure.

Contrastingly, an elevation of the magnetic parameter yields a modest improvement in Nu_{Avg} and a more pronounced escalation in total entropy production. The increment in the magnetic parameter generates a secondary body force, serving to invigorate the fluid circulation within the enclosure. This revitalized fluid motion contributes positively to enhanced heat transfer, manifesting in the increased Nu_{Avg} and entropy production.

Fig. 14 offers contour maps that delineate key field parameters, namely temperature, phase transition, local entropy generation, and flow streamlines, each corresponding to diverse Hartmann numbers. As Ha rises, a palpable shift in the temperature contours occurs, moving them away from the cold wall and closer to the magnetic source. This shift can be ascribed to the resistive velocity forces emanating from the magnetic source, which significantly influence the area between the cold wall and itself. Additionally, the isotherms near the hot wall also shift toward the magnetic source in the upper regions, resulting in a marginal diminution of temperature gradients and, as corroborated by Fig. 13, a consequent reduction in Nu_{Avg}.

The investigation reveals that when the Hartmann number is incrementally increased from an initial state of zero to a subsequent value of 60, a significant decrease in the average Nusselt number is observed. Specifically, the Nu_{Avg} falls from an initial value of 3.04 down to 2.46, translating to a notable reduction of 19 %. This suggests that a higher Hartmann number, generally indicative of a more substantial magnetic field, tends to inhibit the convective heat transfer rate.

Additionally, the research indicates a significant reduction in the system's total entropy generation when the Hartmann number is increased to 60. As a metric of irreversible losses in thermodynamic processes, the total entropy generation sees a decrease of 26 %. An uptick in *Ha* induces a slight repositioning of the phase transition region toward the magnetic source. This spatial adjustment can be directly linked to the observed shifts in the temperature profile as evident in the isotherm contours. Moreover, higher *Ha* values are associated with a decline in local entropy generation adjacent to the cold wall and magnetic source. This local decrease culminates in an overarching reduction of total entropy generation, as previously highlighted in Fig. 13.

Fig. 15 illustrates how variations in the Rayleigh number (*Ra*) and the thermal conductivity ratio (R_k) influence two critical parameters: the average Nusselt number (Nu_{Avg}) and the total entropy generation (ET). The ratio of thermal conductivity, R_k, measures the thermal conductivity of the solid wall relative to the base fluid. Increasing the thermal conductivity of the wall enhances the heat distribution efficiency across both the hot and cold walls. Notably, higher values of both *Ra* and R_k lead to increases in Nu_{Avg} and E_T. When the wall's thermal conductivity equals that of the fluid suspension ($R_k = 1$), the effect of an increased *Ra* on Nu_{Avg} becomes less pronounced. Under these conditions, the lower thermal conductivity of the wall acts as a limiting factor, restricting enhancements in heat transfer.

Contrastingly, when R_k escalates to 100, an incremental increase in *Ra* causes a nearly linear, and substantial, surge in Nu_{Avg}. Under these conditions, convective heat transfer within the enclosure becomes the

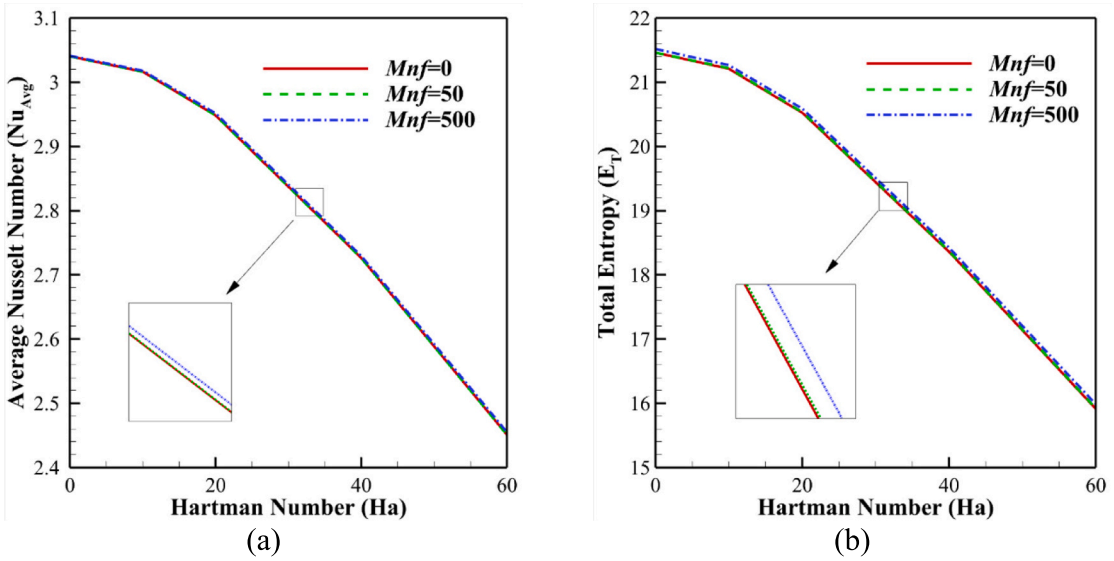

Fig. 13. Effect of Hartman number for various values of Magnetic number (*Mnf*) on (a) Average Nusselt number, and (b) Total entropy.

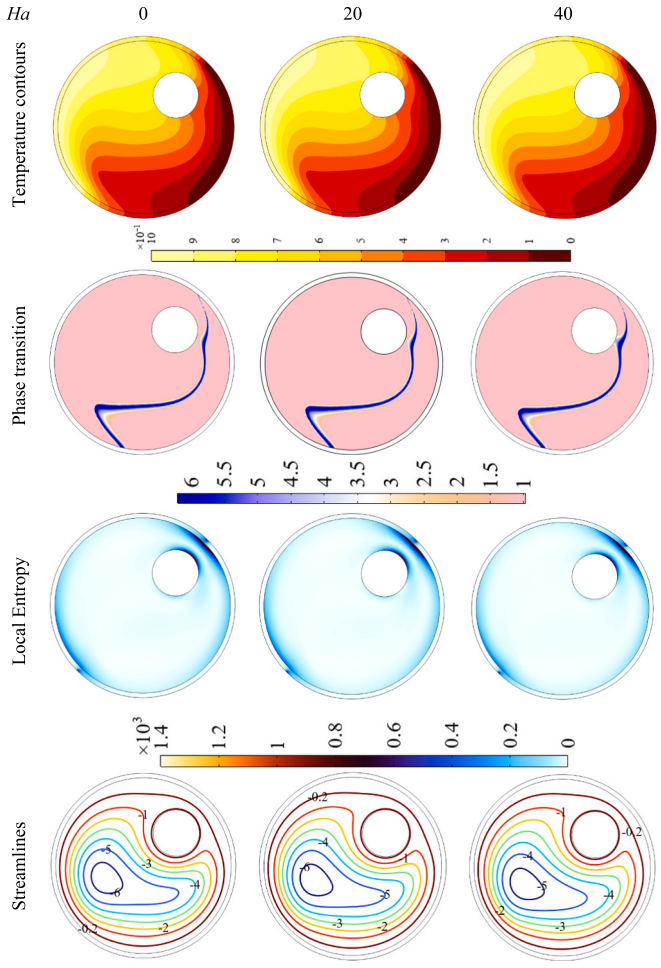

Fig. 14. Effect of Hartman number contour maps of key parameters.

dominant heat transfer mechanism. This convective influence is magnified by increasing *Ra*, thus contributing to both heightened heat transfer rates and subsequent entropy generation. At a Ra = 100,000, an increase of R_k from 1 to 100, rises Nu_{Avg} from about 2 to about 4.5. Thus, a 56 % enhancement in Nu_{Avg} can be obtained by variation of thermal conductivity ratio.

Fig. 16 elaborates on the spatial distribution of key field parameters, captured through contour maps for various *Ra* values. For low *Ra* (*Ra* = 1000), the isotherms manifest a linear pattern, extending uniformly from the hot to the cold wall. With the amplification of *Ra* to 10,000, noticeable distortions in the isotherms become apparent, largely attributable to natural convection currents. Under this condition, the flow streamlines intensify, and evidence of free convection circulations emerges between the magnetic source and the cold wall.

Further escalation of *Ra* introduces more pronounced isothermal distortions and a propensity for streamlines to drift toward the hot wall, a region free from magnetic interference, thereby enabling uninhibited fluid circulation. Moreover, an increasing *Ra* also repositions the phase transition zone, nudging it closer to the hot wall. This effect is most marked at Ra = 100,000, where the contours of phase transition (*Cr*) closely shadow the corresponding isotherms, particularly near the temperature θ_f. Such behavior arises because the isotherms, deflected by free convection currents, inherently guide the phase transition zones. Consistent with the observations made in Fig. 15, these trends collectively result in enhanced local entropy generation adjacent to the hot and cold walls, culminating in a net increase in total entropy production.

Fig. 17 illustrates the subtle impacts of varying the fusion temperature of nanoparticles (θ_f) on the local Nusselt number (Nu_L) along the enclosure's hot wall. It is noted that an increase in the fusion temperature leads to a slight improvement in Nu_L, especially in the middle section of the hot wall.

In Fig. 18, the analysis of phase transition maps (*Cr*) indicates that an increase in θ_f shifts the phase transition zone closer to the hot wall. This movement has a series of thermal effects: it intensifies the temperature gradients adjacent to the hot wall, which in turn indirectly boosts the local Nusselt number (Nu_L). This increase in the local Nusselt number is indicative of enhanced heat transfer efficiency near the hot wall due to the heightened thermal gradients.

Furthermore, the adjustment in θ_f also subtly impacts the internal flow dynamics within the enclosure. It leads to minor yet noticeable deformations in the isotherms, which are expected to alter the flow characteristics. Although these isotherm deformations suggest changes in thermal distribution, they are not pronounced enough to cause significant alterations in the flow streamlines. These nuanced changes are important for understanding the complex interplay between thermal and flow dynamics in the system, as illustrated in Fig. 18.

Moreover, because the impact of θ_f on both the isotherms and flow

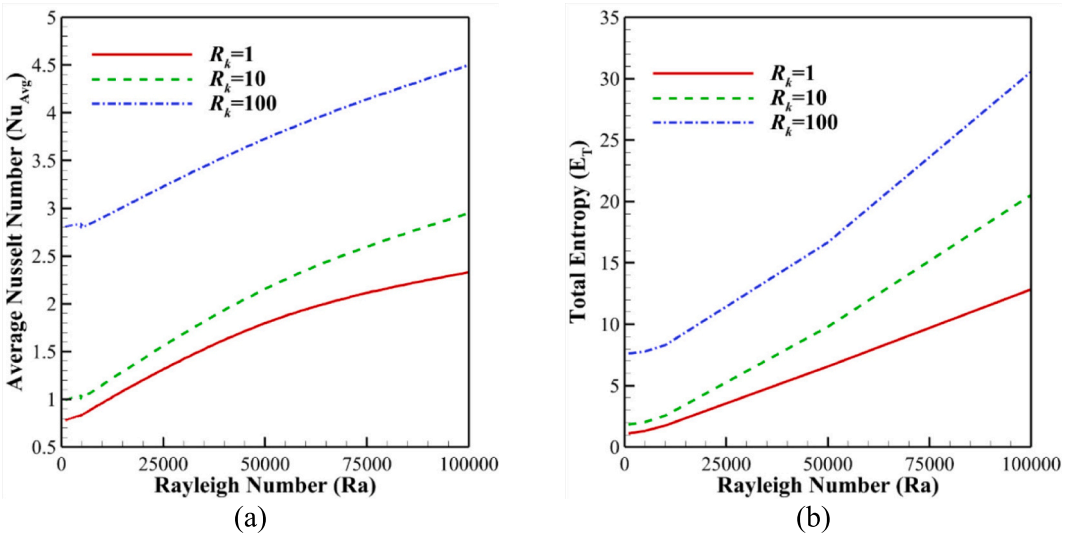

Fig. 15. Effect of Rayleigh number (*Ra*) for various values of R_k on (a) Average Nusselt number, and (b) Total entropy.

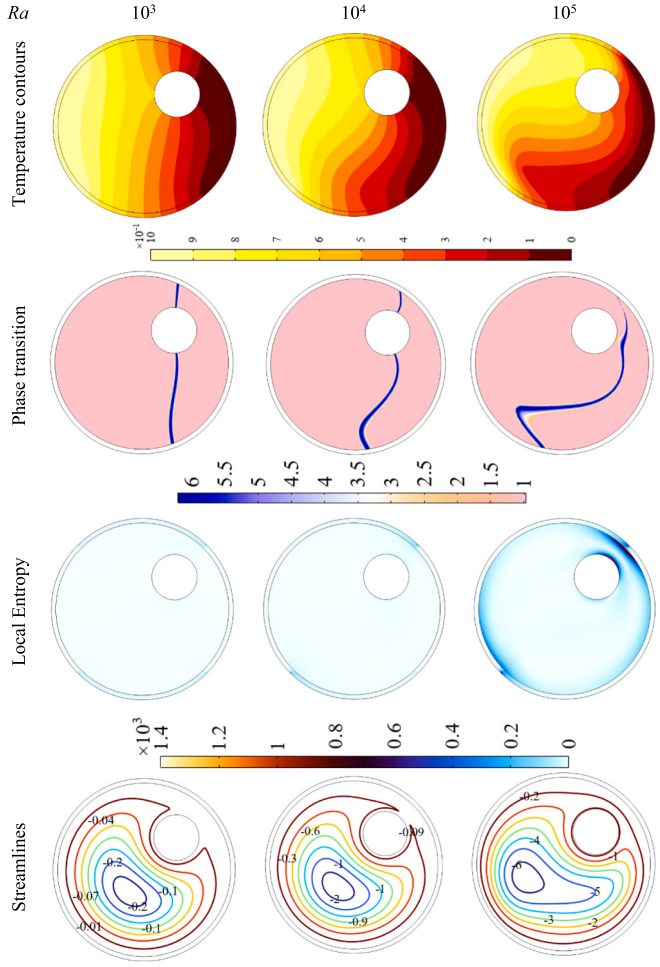

Fig. 16. Effect of Rayleigh number contour maps of key parameters.

streamlines remains minimal, there is an absence of dramatic shifts in local entropy generation contours. In other words, the topography of local entropy generation remains largely unchanged across different θ_f values. This indicates that the fusion temperature of nanoparticles exerts its most significant influence on heat transfer metrics like Nu_L, while

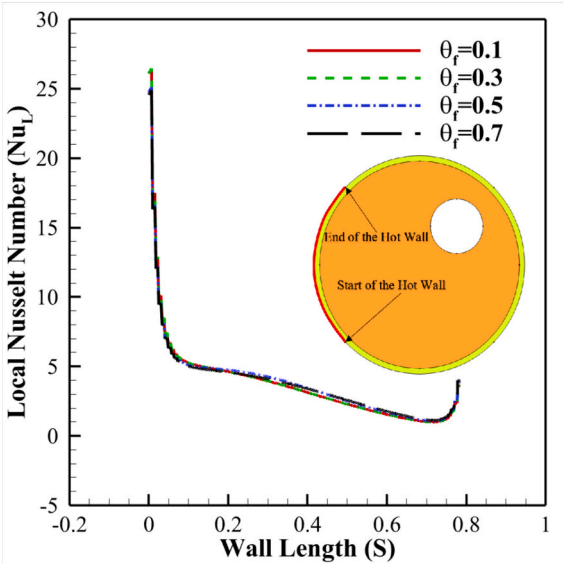

Fig. 17. Effect of θ_f on the local Nusselt number (Nu_L).

leaving the fluid dynamics and entropy generation largely unperturbed.

Fig. 19 meticulously examines the impact of nanoparticle fraction on the local Nusselt number (Nu_L), particularly focusing on its effects near the bottom-middle portion of the hot wall. It is revealed that elevating nanoparticle concentration leads to an augmentation in Nu_L in this specific region of the hot wall. Turning our attention to Fig. 20, which presents isotherm configurations, a subtle migration of these isotherms toward the bottom-middle section of the hot wall is noticeable. This shift has a consequential impact on the phase transition maps (*Cr*), driving them closer to the hot wall as well. At the root of these observable shifts is a key thermophysical phenomenon: the enhancement of the suspension's thermal conductivity with the inclusion of higher nanoparticle concentrations. Improved thermal conductivity amplifies the overall rate of heat transfer, thus directly influencing the local Nusselt number and indirectly affecting isotherm and *Cr* map placements. It should also be noted different color maps was used for $\varphi = 0.025$ and $\varphi = 0.05$ since the presence of nanoparticles influences the heat capacity ratio notably.

Furthermore, the nanoparticle concentration has a nuanced effect on the fluid streamlines within the enclosure. Although the changes are

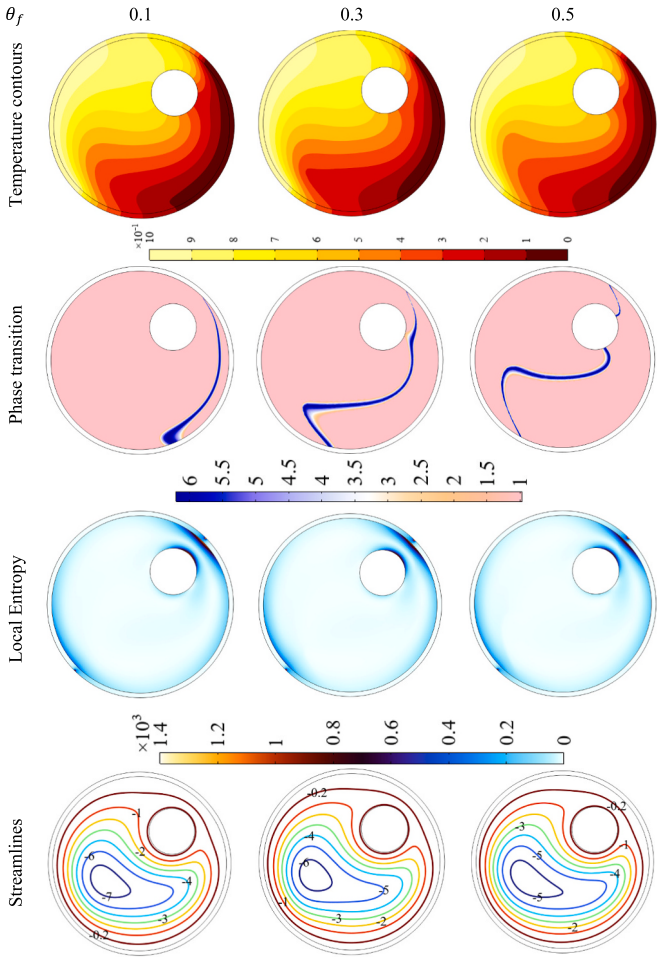

Fig. 18. Effect of Rayleigh number contour maps of key parameters.

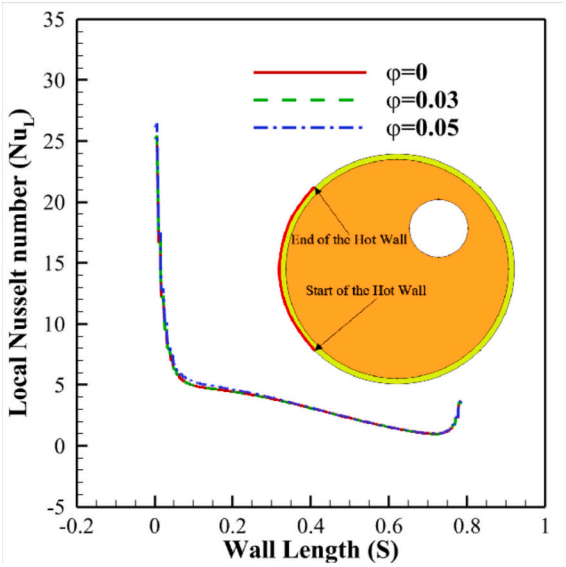

Fig. 19. Effect of the volume fraction of the nanoparticles (φ) on the local Nusselt number (Nu_L).

subtle, they are worth noting. Specifically, the fluid streamlines exhibit slight alterations due to the improved heat transfer dynamics brought about by the increased nanoparticle concentration. Lastly, a careful

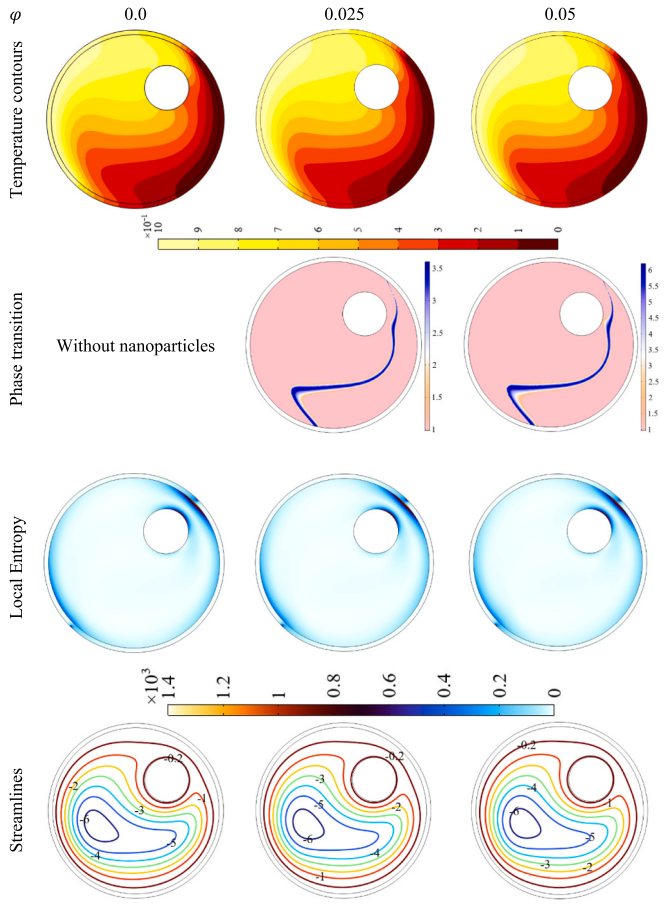

Fig. 20. Effect of nanoparticles concentration on contour maps of key parameters.

examination of local entropy generation patterns unveils a modest shift toward the enclosure's center, moving away from the walls. This migration can be attributed to enhanced heat transfer rates, which occur when nanoparticle concentration rises. Essentially, the higher the nanoparticle concentration, the better the heat transfer, resulting in a redistribution of local entropy generation within the enclosure.

4.2. *Artificial intelligence study of the model*

In this article, an Adaptive Network-Based Fuzzy Inference System (ANFIS) is used to predict the average Nusselt number. ANFIS is a hybrid intelligent system that combines the learning capabilities of neural networks with the fuzzy logic qualitative approach. The system leverages the strengths of both techniques to model complex, nonlinear relationships. The primary components of ANFIS include:

- Fuzzy Inference System (FIS): This involves defining fuzzy rules and membership functions to capture the expert knowledge in a rule-based system.
- Artificial Neural Network (ANN): This provides the ability to learn from data and adjust the fuzzy rules and membership functions accordingly.

By integrating these components, ANFIS can adaptively learn from the data and improve its prediction accuracy over time.

The ANFIS integrates the strengths of fuzzy logic and neural networks, creating a powerful tool for modeling complex, nonlinear systems. The architecture of ANFIS as depicted in Fig. 21 is designed as a multilayer feed-forward network, where each layer performs a specific role in processing inputs and generating outputs. It consists of five

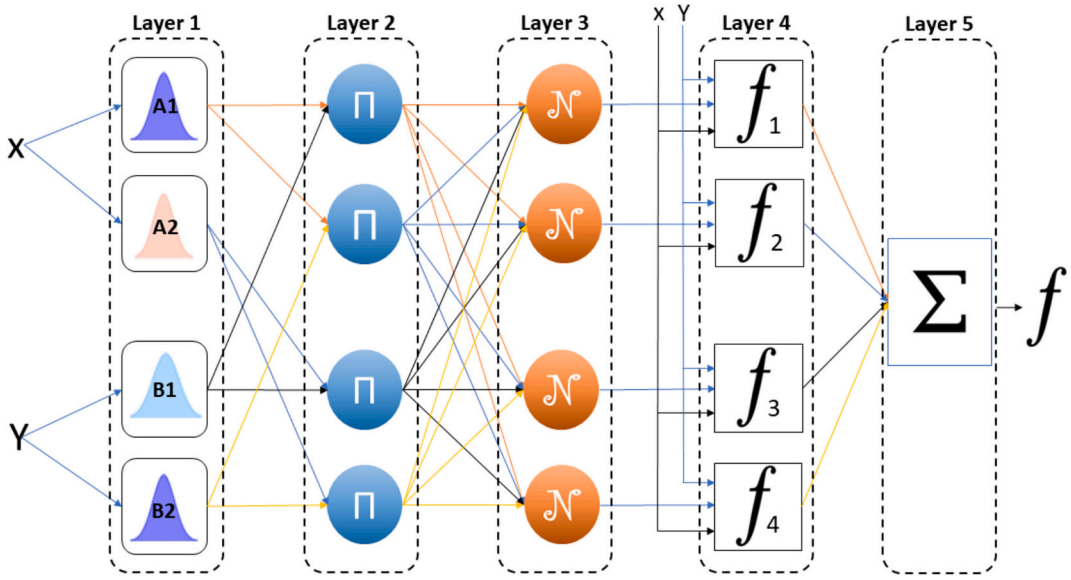

Fig. 21. ANFIS architecture.

distinct layers, each contributing to the overall functionality of the system. These layers are: the fuzzy layer, the rule layer, the normalization layer, the defuzzification layer, and the output layer. Only layer 1 (fuzzy layer) and layer 4 (defuzzification layer) have trainable parameters that must be tune during training process. In Fig. 1, for simplicity in illustrating the structure of ANFIS, only two inputs, X and Y, and four membership functions, A_1, A_2, B_1, and B_2, are shown. However, in this article, there are six inputs, and five membership functions are added for each input.

Layer 1: Fuzzy layeris responsible for the fuzzification of input variables. The fuzzification process involves applying membership functions to the inputs to convert crisp values into fuzzy values. Common membership functions used include bell-shaped functions and Gaussian functions. For each input such as x, output of membership function A_i is calculated as:

$$O_i^1 = \mu_{A_i}(x) \tag{36}$$

The formulation of bell-shaped function would be:

$$\mu_{A_i}(x) = \frac{1}{1+\left[\left(\frac{x-c_i}{a_i}\right)^2\right]^{b_i}} \tag{37}$$

Gaussian is another popular membership function that is defined as following formulation:

$$\mu_{A_i}(x) = exp\left(-\left(\frac{x-b_i}{a_i}\right)^2\right) \tag{38}$$

That a_i, b_i, and c_i are the trainable parameters that must be tuned and determine the shape of membership function. In this article, Gaussian membership function is used.

Layer 2: rule layer establishes the fuzzy rules that define the relationships between input variables. Each node receives output values of the first layer and represents the fuzzy rules of the respective input values. The output of i^{th} node of Layer 2, so-call firing strength, is calculated as following equation:

$$O_i^2 = w_i = \mu_{A_i}(x) \times \mu_{B_i}(x) \tag{39}$$

Any operator that performs a fuzzy AND rule such as minimum can be used as a nod function. If minimum use as nod operator, output of Layer 2 calculated as:

Table 3
Dataset Variables Properties.

Dataset Variables			Range
	Symbol	Description	
Input data	*Ra*	Rayleigh number	0 – 1E5
	Mnf	Magnetic Parameter	0–500
	Ha	Hartmann number	0–60
	R_K	Thermal conductivity ratio	1–100
	θ_f	Fusion temperature	0.1–0.9
	φ	NEPCM volume fraction	0–0.05
Output data	Nu_{Avg}	Average Nusselt number	0.7–4.45

$$O_i^2 = w_i = min\left(\mu_{A_i}(x), \mu_{B_i}(x)\right) \tag{40}$$

In this article we use Eq. (39).

Layer 3: Normalization layer normalizes the firing strengths from the rule layer. The nodes in this layer compute the ratio of each rule's firing strength to the total firing strengths of all rules. This ensures that the sum of the normalized firing strengths is equal to one. So, the performance of this layer can be formulated as the following equation:

$$O_i^3 = \overline{w}_i = \frac{w_i}{\sum_j w_j} \tag{41}$$

Layer 3 does not have any trainable parameters.

Layer 4: Defuzzification layer receives normalized firing strengths ($\overline{w}_i$) as well as the original inputs (X and Y) and returns weighted values of each rule's node by:

$$O_i^4 = \overline{w}_i(p_i x + q_i y + r_i) = \overline{w}_i f_i \tag{42}$$

p_i, q_i, and r_i are tunable parameters that must be tuned during training process.

Layer 5: Output layer is the final layer and aggregates the outputs from the defuzzification layer to produce the overall ANFIS output. The final output is given by:

$$O^5 = f = \sum_i \overline{w}_i f_i \tag{43}$$

We developed a dataset from seven unique melting scenarios, generating 5000 samples from simulated data. We provided the dataset here https://data.mendeley.com/preview/5pjf454xts?a=fb80d93

Table 4
Dataset variables properties.

Data Type	MSE (Loss value)	Mean absolute error
Training Data	4.35e-5	4.5e-3
Validation Data	7.3e-5	5.53e-3
Test Data	8.245e-5	5.5e-3

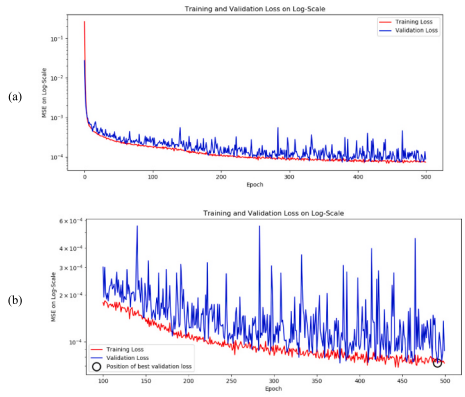

Fig. 22. The model training history and fitness: (a) Training and validation data over different epochs; (b) Training and validation data from epoch 100 to 500.

e-9046-4768-8c96-d139ab78638d

Thus, future researchers can use the dataset to develop or test new neural network models and analyze the results further. The dataset's input and output variables are itemized in Table 3, along with the span of values for each input parameter.

Before the start of the training phase, the dataset underwent a normalization and shuffling process, allocating 70 % for training while the rest was split equally for validation and testing. The objective of the training was to reduce the Mean Squared Error (MSE) through the application of the Adam optimizer [53], conducted over 500 episodes with batch sizes set to one. Five Gaussian membership functions were added for each input, and validation data utilized during the training to mitigate overfitting risks. The data was standardized using the StandardScaler method [54].

The results of the training for all parts of dataset are displayed in Table 4. The table notes that the validation loss was recorded at 7.3e-5, and the testing loss at 8.245e-5, both figures indicating high accuracy of the training and model due to their minimal values. Fig. 22 displays the reduction in MSE over various epochs for both training and validation sets, showing continuous improvement. Specifically, Fig. 22 (a) covers all epochs while Fig. 22 (b) focuses on the decline in error from epoch 100 to 500 and highlights the epoch with the optimal validation loss at 491, suggesting that further training could potentially lower validation losses even more.

Fig. 23 illustrates the comparison between the actual outcomes and the predictions made by the model for the test data, with an R^2 value of 0.9999, demonstrating the model's precision. The predictions closely match the actual data points, as seen in Fig. 23 (a), with predicted values nearly identical to actual measurements. Fig. 23 (b) plots actual and predict value of 100 randomly selected test data points, showcasing that the predictions closely align with the true values. The adeptness of the ANFIS in making precise predictions allowed for the accurate and fast calculation of average Nusselt number. Running many cases for a combination of control parameters can results in contours for behavior of average Nusselt number (Nu_{Avg}). Fig. 24 displays the membership functions post-training for all inputs.

Figs. 25–28 show contours of average Nusselt number dependent on the train data range of the interest parameters and numbers, means the nanoparticles concentration (φ), thermal conductivity ratio (R_k), magnetic number (Mnf), Rayleigh number (Ra), and the fusion temperature (θ_f) parameter. According to the obtained results in Fig. 25, both of the thermal conductivity ratio (R_k) and the nanoparticles concentration (φ) have positive impression on the average Nusselt number contours. When R_k increases, the conduction mode will be dominant throughout the enclosure. Hence, the heat transfer rate is augmented. Since the presence of the nanoparticles improves the local heat capacity locally, the average Nusselt number is increased by adding a more portion of the nanoparticles. Figs. 26 and 27 explain that average Nusselt number contours are under weak influence of the magnetic source strength; so that, the contours have gotten the vertical and the horizontal patterns in Figs. 26

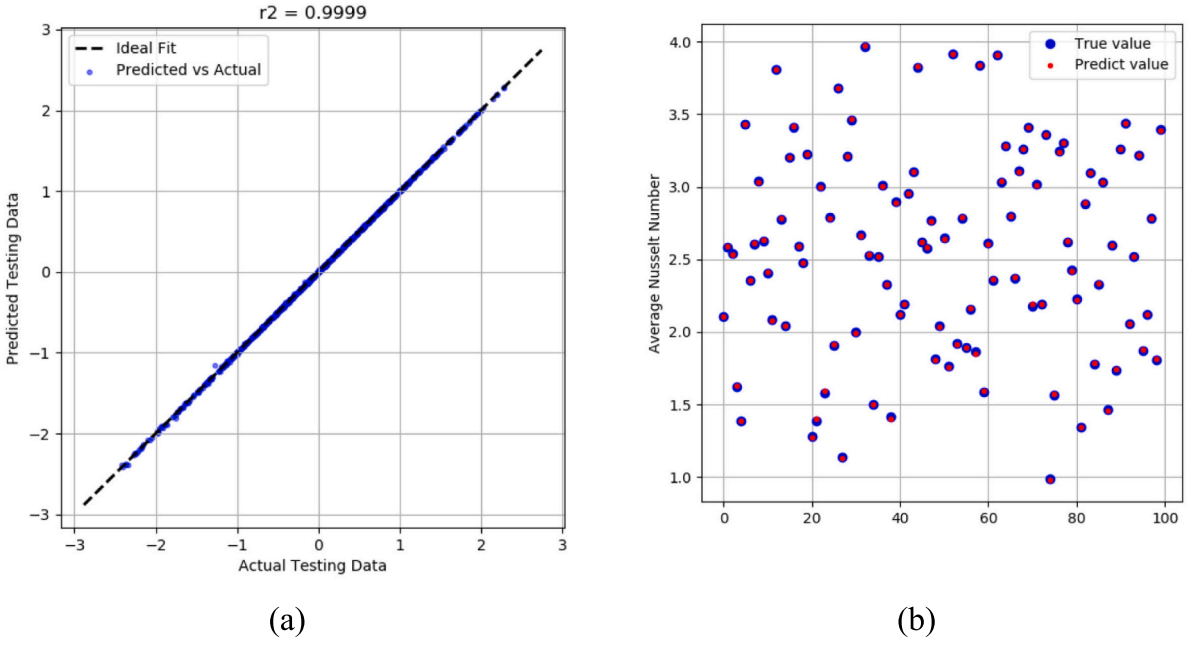

Fig. 23. Comparison between actual test results and predicted values (a) axis x is actual testing data and axis y is predicted values (b) plot true and predict value of 100 random test data (Un-normal value).

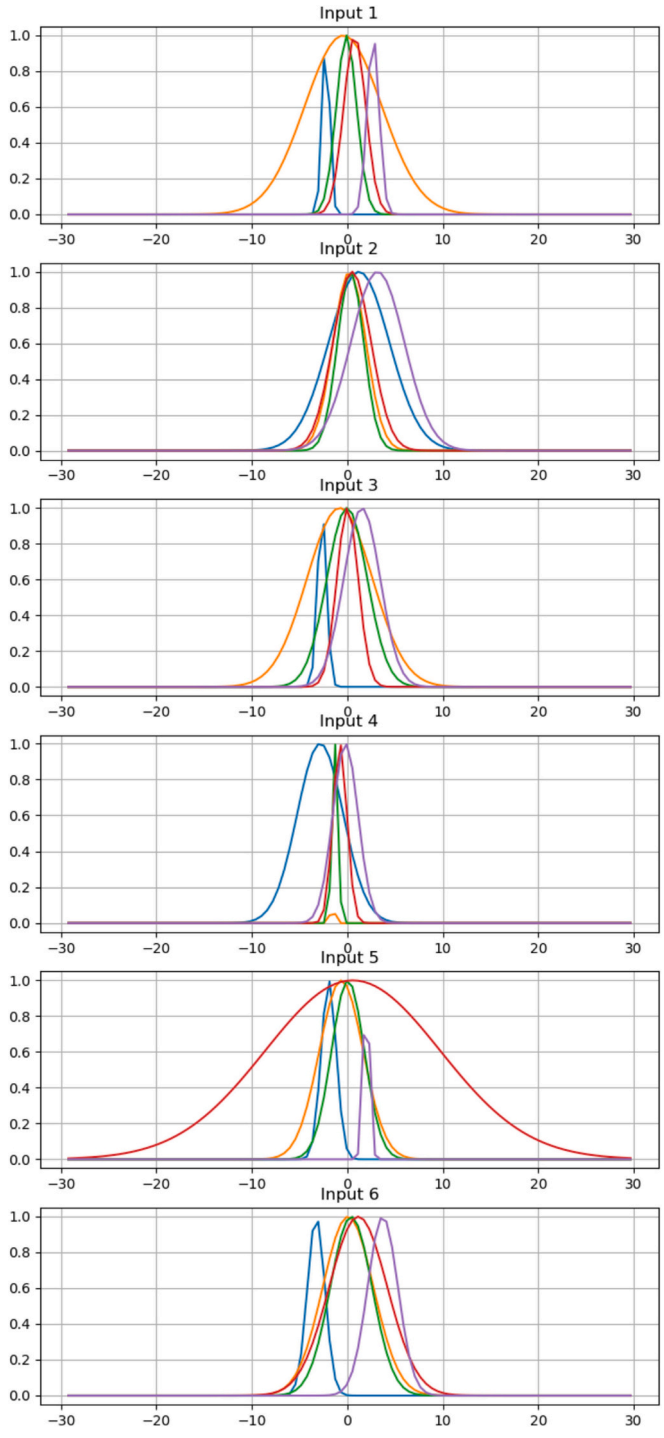

Fig. 24. Membership functions for all inputs after training process.

and 27, respectively. The default position of the sleeve (position 2 defined in Fig. 7) has a direct impression on the depicted patterns. It is worth to note that the sleeve is far from the hot left wall, where the average Nusselt number is evaluated; hence, even the most powerful magnetic source ($Mnf = 500$) cannot be effective on the rate of heat transfer. As referred, regarding the proposed physical model, the thermal conductivity ratio (R_k), has always a positive effect on the average Nusselt number contours. So, the obtained patterns in Fig. 26 are generally vertical with an increment from left to right side. In contrast, augmentation of Rayleigh number (Ra), by creating a robust convective suspension, improves average Nusselt number contours from downward to upward (see Fig. 27). An approximately non- linear pattern for the

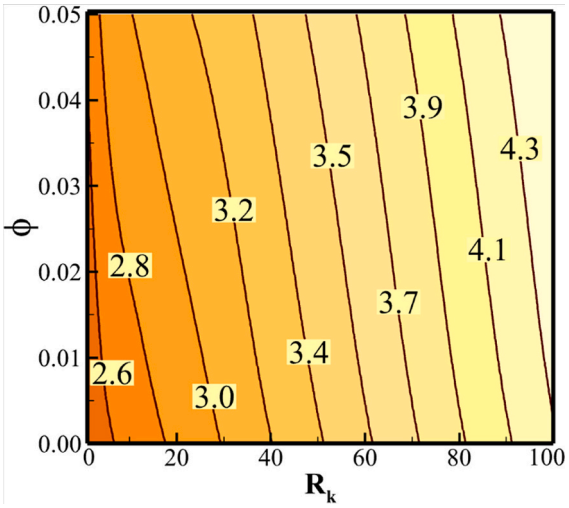

Fig. 25. Average Nusselt number contours as function of the thermal conductivity ratio and the nanoparticles concentration, in the range of train data.

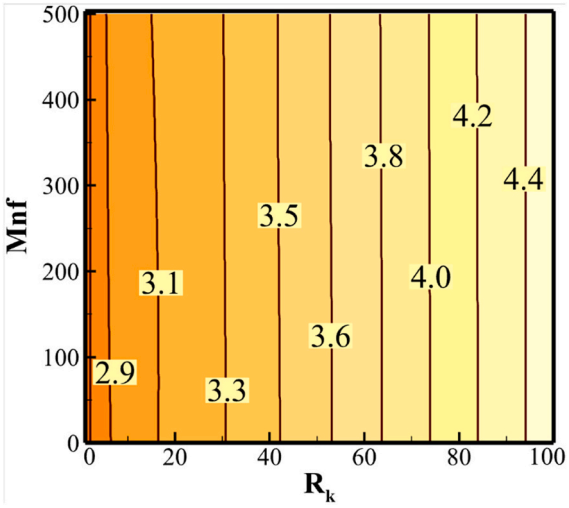

Fig. 26. Average Nusselt number contours as function of magnetic number and thermal conductivity ratio, in the range of train data.

average Nusselt number contours can be observed in Fig. 28. A large gap, where the maximum value of the average Nusselt number is evaluated, has just been appeared in the center region of Fig. 28. It shows the optimum value of the average Nusselt number is occurred in the range of $0.35 \leq \theta_f \leq 0.75$. Indeed, below and top contours of the referred gap could not reach to this maximum value. Apart from the effect of fusion temperature (θ_f) on the average Nusselt number contours, a neglect impression through magnetic number (Mnf) on the contours is still remained.

5. Conclusion

The current research conducts a detailed examination of the complex heat and mass transfer behaviors within an enclosure containing NEPCM suspension, influenced by magnetic fields. By employing a set of governing PDEs, the study establishes a mathematical model that encompasses natural convection, convective heat transfer within the NEPCM domain, and conjugate heat transfer across the solid boundaries. This model promotes a thorough exploration of fluid dynamics, latent heat energy storage, and the melting and solidification dynamics. Additionally, the research incorporates an analysis of entropy production,

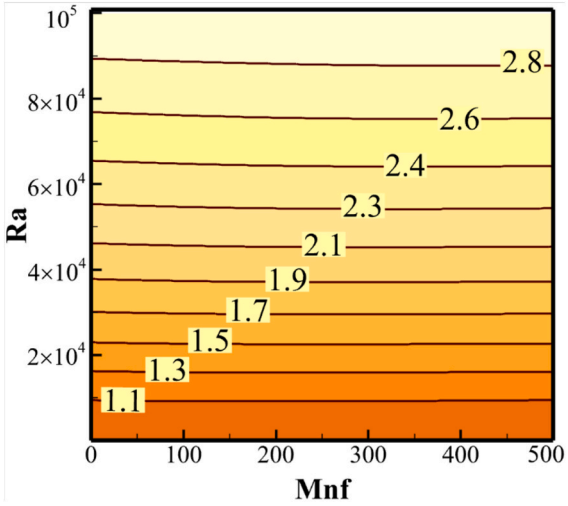

Fig. 27. Average Nusselt number contours as function of magnetic number and Rayleigh number, in the range of train data.

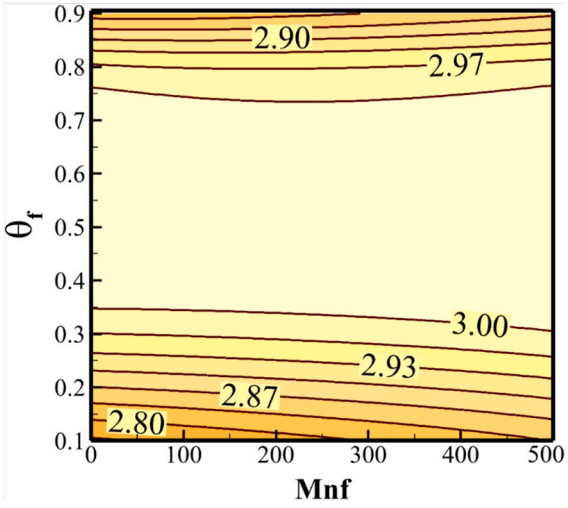

Fig. 28. Average Nusselt number contours as function of magnetic number and fusion temperature, in the range of train data.

categorizing it into thermal and frictional types. The dimensionless forms of these equations were resolved using FEM. A neural network was utilized to learn the impact of parameters on the Nu_{Avg}. Then, the trained model was used to provide contours of parameters influence on the average Nusselt number. The effects of various parameters, including the magnetic number, Hartmann number, Rayleigh number, thermal conductivity ratio, nanoparticles fusion temperature, and nanoparticle concentration, were methodically evaluated in terms of their impact on heat transfer, entropy generation, and field contours. A key finding of this study highlights the significant role of the magnetic source's placement in influencing both heat transfer and entropy generation. The primary outcomes of this investigation are summarized as follows:

- A pronounced impact on the local Nusselt number (Nu_L) was observed when the magnetic source was located at the bottom-left quadrant. In this position, Nu_L was dampened at the midpoint of the hot wall's length, demonstrating the significant role of the magnetic source in directing fluid flow and consequently influencing heat transfer.
- An increase in the Hartmann number led to a 19 % reduction in the average Nusselt number (Nu_{Avg}) from 3.04 to 2.46 and a 26 % decrease in total entropy generation (E_T). Conversely, elevating the magnetic number marginally improved Nu_{Avg} and substantially increased E_T.
- At Ra = 100,000, increasing R_k from 1 to 100 resulted in a Nu_{Avg} boost from 2 to 4.5, reflecting a 56 % enhancement.
- Enhanced Nu_L was noted near the bottom-middle section of the hot wall, correlating with higher nanoparticle concentrations, which is ascribed to the improved thermal conductivity of the NEPCM suspension.
- Regions of high entropy generation were consistently observed close to the magnetic source, regardless of its specific location, suggesting zones of extended temperature gradients and reduced entropy generation.
- Higher *Ra* and R_k values were associated with enhanced heat transfer rates and phase transition zones moving closer to the hot wall, confirming their synergistic effects on heat and mass transfer phenomena.
- The selected position of the magnetic source causes an insignificant effect of the magnetic number on the average Nusselt number contours. The thermal conductivity ratio (R_k) and Rayleigh number (*Ra*) due to improve in conduction and convection modes, increase the average Nusselt number contours, respectively. Fusion temperature (θ_f) has not a linear impression on the average Nusselt number contours since the most powerful contours have been stated in the range of $0.35 \leq \theta_f \leq 0.75$.

In the present study, isotherm boundary conditions were applied. The presence of NEPCM particles forms a phase change region in the domain and regulates the heat flux flow. In many applications, such as solar tubes or heat sinks, heat flux boundary conditions are required. In these cases, NEPCM particles may be effective in controlling surface temperatures. The impact of NEPCM particles on temperature regulation and entropy generation can be the subject of future studies.

CRediT authorship contribution statement

Hakim S. Sultan Aljibori: Writing – original draft, Resources, Methodology, Investigation, Formal analysis, Data curation, Conceptualization. **Mohammed Hasan Ali:** Writing – original draft, Visualization, Methodology, Investigation. **Zehba Raizah:** Writing – original draft, Resources, Methodology, Investigation, Funding acquisition. **Ahmad Hajjar:** Writing – review & editing, Writing – original draft, Visualization, Software, Investigation. **Jana Shafi:** Writing – review & editing, Writing – original draft, Visualization, Validation, Software, Resources, Investigation. **Faisal Alresheedi:** Writing – review & editing, Writing – original draft, Resources, Methodology, Investigation, Data curation, Conceptualization. **Ahmed Elhassanein:** Writing – review & editing, Writing – original draft, Resources, Investigation, Funding acquisition, Formal analysis, Data curation. **Mohammad Edalatifar:** Writing – review & editing, Writing – original draft, Visualization, Validation, Software, Resources, Investigation. **Mohammad Ghalambaz:** Writing – review & editing, Writing – original draft, Supervision, Methodology, Conceptualization.

Declaration of competing interest

The authors clarify that there is no conflict of interest for report.

Acknowledgements

The authors are thankful to the Deanship of Graduate Studies and Scientific Research at University of Bisha for supporting this work through the Fast-Track Research Support Program. The authors extend their appreciation to the Deanship of Research and Graduate Studies at

King Khalid University for funding this work through large Research Group Project under the grant number (RGP2/198/45).

Data availability

The dataset is placed on Mendely and the link to the dataset has been provided inside the manuscript.

References

[1] M. Bahiraei, S. Heshmatian, Electronics cooling with nanofluids: a critical review, Energy Convers. Manag. 172 (2018) 438–456.
[2] S. Chavan, R. Rudrapati, S. Manickam, A comprehensive review on current advances of thermal energy storage and its applications, Alex. Eng. J. 61 (7) (2022) 5455–5463.
[3] S. Preetam, B.K. Nahak, S. Patra, D.C. Toncu, S. Park, M. Syväjärvi, G. Orive, A. Tiwari, Emergence of microfluidics for next generation biomedical devices, Biosens. Bioelectron. X 10 (2022) 100106.
[4] Q. Wang, L. Yang, J. Song, Preparation, thermal conductivity, and applications of nano–enhanced phase change materials (NEPCMs) in solar heat collection: a review, J. Energy Storage 63 (2023) 107047.
[5] M.S. Ghoghaei, A. Mahmoudian, O. Mohammadi, M.B. Shafii, H. Jafari Mosleh, M. Zandieh, M.H. Ahmadi, A review on the applications of micro−/nano-encapsulated phase change material slurry in heat transfer and thermal storage systems, J. Therm. Anal. Calorim. 145 (2021) 245–268.
[6] C. Ho, Y.-C. Liu, M. Ghalambaz, W.-M. Yan, Forced convection heat transfer of Nano-encapsulated phase change material (NEPCM) suspension in a mini-channel heatsink, Int. J. Heat Mass Transf. 155 (2020) 119858.
[7] B. Jalili, S. Sadighi, P. Jalili, D.D. Ganji, Numerical analysis of MHD nanofluid flow and heat transfer in a circular porous medium containing a Cassini oval under the influence of the Lorentz and buoyancy forces, Heat Transf. 51 (7) (2022) 6122–6138.
[8] M. Sathiyamoorthy, A.J. Chamkha, Natural convection flow under magnetic field in a square cavity for uniformly (or) linearly heated adjacent walls, Int. J. Numer. Methods Heat Fluid Flow 22 (5) (2012) 677–698.
[9] J.T. Cieśliński, M. Fabrykiewicz, Thermal energy storage with PCMs in Shell-and-tube units: a review, Energies 16 (2) (2023) 936.
[10] M. Rashidi, I. Mahariq, M. Alhuyi Nazari, O. Accouche, M.M. Bhatti, Comprehensive review on exergy analysis of shell and tube heat exchangers, J. Therm. Anal. Calorim. 147 (22) (2022) 12301–12311.
[11] A.I. Alsabery, A.S. Abosinnee, S.K. Al-Hadraawy, M.A. Ismael, M.A. Fteiti, I. Hashim, M. Sheremet, M. Ghalambaz, A.J. Chamkha, Convection heat transfer in enclosures with inner bodies: a review on single and two-phase nanofluid models, Renew. Sust. Energ. Rev. 183 (2023) 113424.
[12] A. Alsabery, H. Kadhim, M. Ismael, I. Hashim, A. Chamkha, Impacts of amplitude and heat source on natural convection of hybrid nanofluids into a wavy enclosure via heatline approach, Waves Random Complex Media 33 (4) (2023) 1060–1084.
[13] A.I. Alsabery, M.A. Ismael, E. Gedik, A.J. Chamkha, I. Hashim, Transient nanofluid flow and energy dissipation from wavy surface using magnetic field and two rotating cylinders, Comput. Math. Appl. 97 (2021) 329–343.
[14] T. Tayebi, F. Dahmane, W. Jamshed, A.J. Chamkha, S.M. El Din, Z. Raizah, Double-diffusive magneto-natural convection of nanofluid in an enclosure equipped with a wavy porous cylinder in the local thermal non-equilibrium situation, Case Stud. Therm. Eng. 43 (2023) 102785.
[15] K. Sudarmozhi, D. Iranian, H. Alhazmi, I. Khan, A. Chandulal, A. Aljohani, A. S. Omer, A. Singh, Effect of heat generation and activation energy on MHD Maxwell fluid with multiple slips, Case Stud. Therm. Eng. 59 (2024) 104424.
[16] S. Karthik, D. Iranian, H. Alhazmi, I. Khan, A. Singh, Heat transfer due to electromagnetic radiation of MHD Powell-Eyring fluid with mass diffusion via lie symmetry scaling, Case Stud. Therm. Eng. 58 (2024) 104348.
[17] K. Sudarmozhi, D. Iranian, H. Alhazmi, I. Khan, A. Aljohani, Computational analysis of MHD channel flow of Maxwell fluid with radiation and chemical reaction effects, Colloid Polym. Sci. (2024) 1–14.
[18] K. Sudarmozhi, D. Iranian, Q.M. Al-Mdallal, Revolutionizing energy flow: unleashing the influence of MHD in the presence of free convective heat transfer with radiation, Int. J. Thermofluids 22 (2024) 100662.
[19] T. Tayebi, A.J. Chamkha, Entropy generation analysis due to MHD natural convection flow in a cavity occupied with hybrid nanofluid and equipped with a conducting hollow cylinder, J. Therm. Anal. Calorim. 139 (3) (2020) 2165–2179.
[20] S.-L. Sun, D. Liu, Y.-Z. Wang, Y.-L. Qi, H.-B. Kim, Convective heat transfer and entropy generation evaluation in the Taylor–Couette flow under the magnetic field, Int. J. Mech. Sci. 252 (2023) 108373.
[21] B. Jalili, A.A. Azar, P. Jalili, D. Liu, M.A. Abdelmohimen, D.D. Ganji, Investigation of the unsteady MHD fluid flow and heat transfer through the porous medium asymmetric wavy channel, Case Stud. Therm. Eng. 61 (2024) 104859.
[22] S. Ahmad, D. Liu, H. Waqas, S. Munir, Numerical simulation of magnetohydrodynamics double-diffusive natural convection in a cavity with non-uniform heated walls, Appl. Therm. Eng. 253 (2024) 123778.
[23] S. Ahmad, D. Liu, S. Yang, Y. Xie, M.S. Khan, M.A. Abdelmohimen, Z. Shah, Shape optimization study for heat and mass transport of magnetic fluid in a closed domain using a nonhomogeneous dynamic model, Case Stud. Therm. Eng. 61 (2024) 104911.
[24] B. Mliki, M.A. Abbassi, Entropy generation of MHD natural convection heat transfer in a heated incinerator using hybrid-nanoliquid, Propuls. Power Res. 10 (2) (2021) 143–154.
[25] A.V. Roşca, N.C. Roşca, I. Pop, M.A. Sheremet, Natural convection and entropy generation in a trapezoidal region with hybrid nanoliquid under magnetic field, Int. J. Numer. Methods Heat Fluid Flow 34 (2) (2023) 429–450.
[26] A.A. Pasha, T. Tayebi, M. MottahirAlam, K. Irshad, A. Dogonchi, A.J. Chamkha, A. M. Galal, Efficacy of exothermic reaction on the thermal-free convection in a nano-encapsulated phase change materials-loaded enclosure with circular cylinders inside, J. Energy Storage 59 (2023) 106522.
[27] S. Hussain, N. Alsedias, A.M. Aly, Natural convection of a water-based suspension containing nano-encapsulated phase change material in a porous grooved cavity, J. Energy Storage 51 (2022) 104589.
[28] A. Alazzam, N.A. Qasem, A. Aissa, M.S. Abid, K. Guedri, O. Younis, Natural convection characteristics of nano-encapsulated phase change materials in a rectangular wavy enclosure with heating element and under an external magnetic field, J. Energy Storage 57 (2023) 106213.
[29] M. Ghalambaz, T. Groşan, I. Pop, Mixed convection boundary layer flow and heat transfer over a vertical plate embedded in a porous medium filled with a suspension of nano-encapsulated phase change materials, J. Mol. Liq. 293 (2019) 111432.
[30] M. Ghalambaz, H. Jin, A. Bagheri, O. Younis, D. Wen, Convective flow and heat transfer of nano-encapsulated phase change material (NEPCM) dispersions along a vertical surface, Facta Universitatis Ser. Mechan. Eng. 20 (3) (2022) 519–538.
[31] Z. Raizah, A.M. Aly, Double-diffusive convection of a rotating circular cylinder in a porous cavity suspended by nano-encapsulated phase change materials, Case Stud. Therm. Eng. 24 (2021) 100864.
[32] A. Alhashash, H. Saleh, Conjugate free convection from an array of discrete heat sources with water and nano-encapsulated phase change particle in a cold enclosure, J. Energy Storage 57 (2023) 106076.
[33] A. Alhashash, H. Saleh, Free convection flow of a heterogeneous mixture of water and nano-encapsulated phase change particle (NEPCP) in enclosure subject to rotation, J. Energy Storage 51 (2022) 104168.
[34] M. Ghalambaz, S.M.H. Zadeh, S. Mehryan, I. Pop, D. Wen, Analysis of melting behavior of PCMs in a cavity subject to a non-uniform magnetic field using a moving grid technique, Appl. Math. Model. 77 (2020) 1936–1953.
[35] M. Sheikholeslami, K. Vajravelu, Nanofluid flow and heat transfer in a cavity with variable magnetic field, Appl. Math. Comput. 298 (2017) 272–282.
[36] M. Ghalambaz, A.J. Chamkha, D. Wen, Natural convective flow and heat transfer of nano-encapsulated phase change materials (NEPCMs) in a cavity, Int. J. Heat Mass Transf. 138 (2019) 738–749.
[37] S. Barlak, O.N. Sara, A. Karaipekli, S. Yapıcı, Thermal conductivity and viscosity of nanofluids having nanoencapsulated phase change material, Nanoscale Microscale Thermophys. Eng. 20 (2) (2016) 85–96.
[38] B. Chen, X. Wang, R. Zeng, Y. Zhang, X. Wang, J. Niu, Y. Li, H. Di, An experimental study of convective heat transfer with microencapsulated phase change material suspension: laminar flow in a circular tube under constant heat flux, Exp. Thermal Fluid Sci. 32 (8) (2008) 1638–1646.
[39] K. Khanafer, K. Vafai, A critical synthesis of thermophysical characteristics of nanofluids, Int. J. Heat Mass Transf. 54 (19–20) (2011) 4410–4428.
[40] L. Chai, R. Shaukat, L. Wang, H.S. Wang, A review on heat transfer and hydrodynamic characteristics of nano/microencapsulated phase change slurry (N/MPCS) in mini/microchannel heat sinks, Appl. Therm. Eng. 135 (2018) 334–349.
[41] H.R. Seyf, Z. Zhou, H. Ma, Y. Zhang, Three dimensional numerical study of heat-transfer enhancement by nano-encapsulated phase change material slurry in microtube heat sinks with tangential impingement, Int. J. Heat Mass Transf. 56 (1–2) (2013) 561–573.
[42] A. Zaraki, M. Ghalambaz, A.J. Chamkha, M. Ghalambaz, D. De Rossi, Theoretical analysis of natural convection boundary layer heat and mass transfer of nanofluids: effects of size, shape and type of nanoparticles, type of base fluid and working temperature, Adv. Powder Technol. 26 (3) (2015) 935–946.
[43] A. Chamkha, A. Doostanidezfuli, E. Izadpanahi, M. Ghalambaz, Phase-change heat transfer of single/hybrid nanoparticles-enhanced phase-change materials over a heated horizontal cylinder confined in a square cavity, Adv. Powder Technol. 28 (2) (2017) 385–397.
[44] A.A. Sakhir Abed, Numerical simulation of laminar incompressible driven cavity flow in a l-shape domain, Int. J. Mechan. Eng. Technol. 10 (1) (2019) 119–132.
[45] S. Mehryan, M. Ghalambaz, L.S. Gargari, A. Hajjar, M. Sheremet, Natural convection flow of a suspension containing nano-encapsulated phase change particles in an eccentric annulus, J. Energy Storage 28 (2020) 101236.
[46] O.C. Zienkiewicz, R.L. Taylor, P. Nithiarasu, The Finite Element Method for Fluid Dynamics, Seventh ed., Butterworth-Heinemann, Oxford, 2014.
[47] D. Pepper, The Intermediate Finite Element Method: Fluid Flow and Heat Transfer Applications, Routledge, 2017.
[48] C.T. Kelley, Solving Nonlinear Equations with Newton's Method, SIAM, 2003.
[49] P. Deuflhard, Newton Methods for Nonlinear Problems: Affine Invariance and Adaptive Algorithms, Springer Science & Business Media, 2005.
[50] M. Bollhöfer, O. Schenk, R. Janalik, S. Hamm, K. Gullapalli, State-of-the-art sparse direct solvers, Parallel Algorithms Comp. Scie. Eng. (2020) 3–33.
[51] M. Bollhöfer, A. Eftekhari, S. Scheidegger, O. Schenk, Large-scale sparse inverse covariance matrix estimation, SIAM J. Sci. Comput. 41 (1) (2019) A380–A401.

[52] T. Kuehn, R. Goldstein, An experimental and theoretical study of natural convection in the annulus between horizontal concentric cylinders, J. Fluid Mech. 74 (4) (1976) 695–719.
[53] I.K.M. Jais, A.R. Ismail, S.Q. Nisa, Adam optimization algorithm for wide and deep neural network, Knowledge Eng. Data Sci. 2 (1) (2019) 41–46.
[54] Scikit-Learn, Sklearn Preprocessing StandardScaler, Scikit-Learn, 2023.